May 15, 2014

PHYS 6016 Final Report - Evolution of the CMS Electromagnetic Calorimeter Endcap Response at the LHC

Adam Butler
University of Southampton, UK

Abstract

Evaluations are made of the likely magnitude of the known response loss mechanisms within the CMS electromagnetic calorimeter endcap at the LHC. Vacuum phototriodes (VPTs) undergo a response loss due to conditioning which is related to the amount of integrated charge taken from the photo-cathode. In order to estimate the integrated charge taken from the photo-cathode an analysis of the anode currents measured in CMS has been undertaken. These measurements, combined with an analysis of the VPT faceplate transmission loss with integrated dose provide input to produce a model for VPT response losses. The CMS Lead Tungstate crystals undergo light yield loss due to high energy hadronic collisions with the crystal lattice nuclei which produce highly ionising fragments that create colour centres in the crystal lattice as they propagate. Light yield losses are also incurred in the crystals from the electromagnetic dose rate, referred to as dE/dx transmission losses, due to the generation of colour centres in the lattice caused by ionisation from the dose rate. An estimate of the hadron damage to the crystals is performed. Extraction of these losses enables the first estimate of the dE/dx crystal transmission losses to be made from CMS in situ data. Predictions of these loss components are made up to the end of Phase 1 LHC running in 2022. As a consequence of this analysis the first observations of the saturation of dE/dx transmission loss at the inner most regions of the endcap calorimeter have been made. The response loss predictions are of great importance to decide whether a full or partial replacement of the electromagnetic calorimeter endcaps will be required for the High Luminosity LHC running after 2022, if the current detector resolution becomes unacceptable.

Contents

1 Introduction

The Endcap Electromagnetic Calorimeter (EE) in the Compact Muon Solenoid (CMS) detector at the Large Hadron Collider (LHC) is constructed from 14,648 lead-tungstate ($PbWO_4$) crystals. Each crystal is mounted with a vacuum phototriode (VPT) on its rear face. The crystals scintillate, producing photons when electromagnetically interacting particles pass through and ionise the crystals. These photons release photo-electrons at the VPT photo-cathode which are then amplified and recorded for physics analysis.

Discussions on the future replacement of the EE are currently ongoing, with concern over the operational lifetime of the present detector. Detector response is decreasing with time, due to transparency losses in the crystals, conditioning losses in the VPTs and VPT faceplate transmission losses. The transparency losses in the crystals are due to ionisation by charged particles called "dE/dx tranmission losses" and transparency losses due to hadron damage. This paper will address these response losses and the consequences for detector resolution and detector replacement.

To predict the VPT conditioning losses, we combine several measurements from CMS data and from laboratory measurements. We use two sources of high voltage monitoring data to measure the current drawn by the VPTs during LHC collisions. These sources are described in Section 2, and we perform cross-checks of the two sets of measurements in Sections 3 and 4. The relationship between the photo-current drawn by individual VPTs to the instantaneous luminosity delivered by the LHC is needed to predict the VPT conditioning losses versus time. This work is described in Sections 5, 6 and 8.

Laboratory measurements of VPT properties and the expected radiation field within CMS are discussed in Section 7. These measurements are used to calculate the VPT current normalisation co-efficient, α, in Section 10. We combine this information with laboratory measurements of VPT conditioning losses versus integrated photo-cathode charge to provide a prediction of the VPT conditioning losses expected as a function of time and detector pseudorapidity. This is described in section 11. Experimental measurements of VPT faceplate transmission losses are discussed in Section 12. Calculations to predict the levels of crystal transparency losses due to hadron damage are described in Section 13.

The EE laser monitoring system measures the combined losses in the detector and is discussed in Section 9. These data are used to determine the proportion of the losses that originate from the VPT conditioning and VPT faceplate transparency loss and the hadronic damage and dE/dx transmission losses in the crystals. The breakdown of the laser monitoring data into the individual response loss components is made in Section 14. Predictions of detector response losses for Phase 1 LHC operation are described in Section 15.

The breakdown of detector response losses allow the first measurements of crystal dE/dx transmission losses to be made in Section 16. This enabled further investigation into dE/dx transmission loss saturation which is discussed in Section 17.

The key physics event for the electromagnetic calorimeter (ECAL) design consideration is the $H \rightarrow \gamma\gamma$ decay. Despite its small branching ratio, the signature of the decay is distinctive. As the width of the Higgs signal is dominated by the two photon mass resolution this makes a high resolution, high granularity calorimeter a key design focus for the ECAL. Finally, the effects of detector response loss on energy resolution will be discussed in Section 18, and the conclusions in Section 19.

1.1 The CMS Experiment

The CMS experiment, shown in Figures 1 and 2, is one of two general purpose high energy particle physics detectors at the Large Hadron Collider. CMS is designed to search for new physics at TeV scales, including the successful search for the Higgs boson, the search for Super Symmetry and dark matter among others. Key to many of these searches, in particular for that of the Higgs boson, is the high resolution electromagnetic calorimeter used to observe, for example, the Higgs to two photon decay [1].

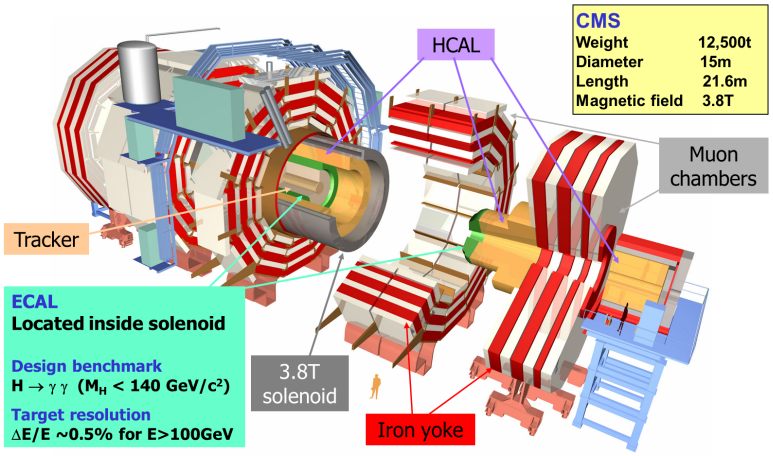

Figure 1: The Compact Muon Solenoid detector at the Large Hadron Collider, CERN.

The detector is 21.6 m in length, 15 m in diameter and features a 3.8 Tesla superconducting solenoid magnet, CMS weighs approximately 12,500 tons. It consists of 5 distinct layers; a tracker, electromagnetic calorimeter, hadronic calorimeter, magnet and muon detector, each split in to a barrel section, covering a pseudorapidity range $-1.5 < \eta < 1.5$, and two endcap sections covering of $1.5 < |\eta| < 3.0$.

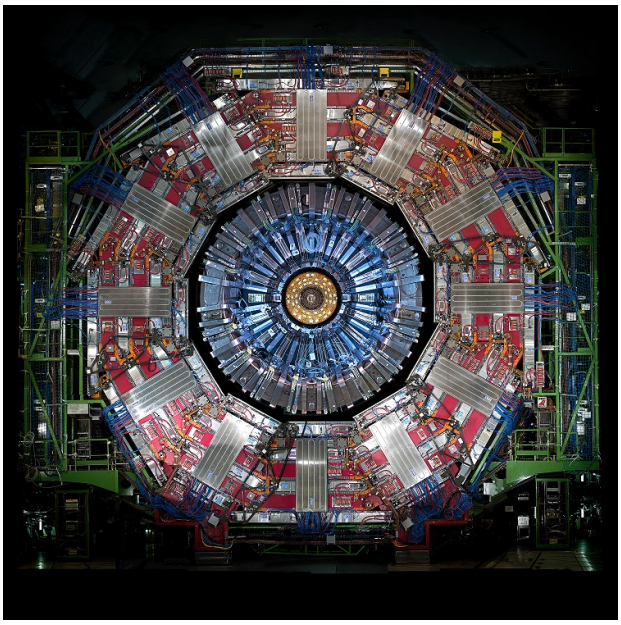

Figure 2: End of view of the CMS detector at the LHC, CERN.

Pseudorapidity (η) is used as a reference scale in this document and is related to the polar spatial co-ordinate within the detector relative to the beam axis. Particle production is relatively constant as a function of pseudorapidity. The electromagnetic calorimeter is subdivided into equal regions of pseudorapidity to ensure even energy distribution flow from minimum bias events into the CMS trigger. Minimum bias events are collisions with small transverse momentum.

Equation 1 describes pseudorapidity as a function of polar angle θ. Figure 3 shows the cross section of the electromagnetic endcap calorimeter relative to the beam axis and interaction point. The bands of pseudorapidity used in later analysis are also shown. Table 1 lists these values of η together with the corresponding values of θ, calculated using Equation 1, and also lists the corresponding radial position at the endcap location.

$$\eta = -\ln\left[\tan\left(\frac{\theta}{2}\right)\right] \tag{1}$$

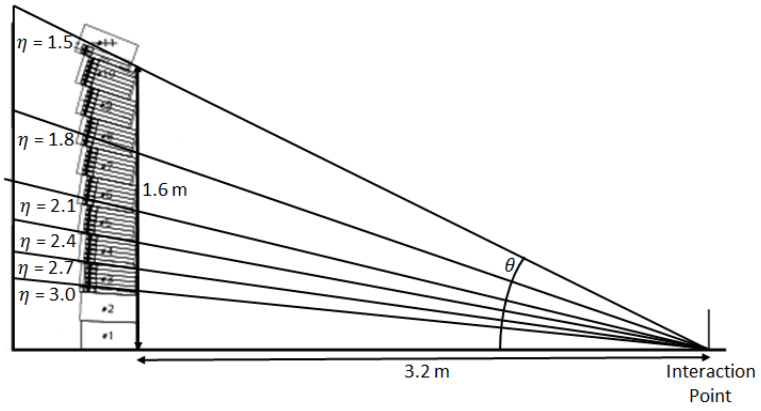

Figure 3: Electromagnetic Endcap calorimeter cross section with the interaction point and bands of 0.3 units of pseudorapidity used in later analysis also shown.

Pseudorapidity, η	Polar Angle, θ (°)	Equivalent Detector Radius (m)
1.5	25.2	1.6
1.8	18.8	1.16
2.1	14.0	0.85
2.4	10.4	0.63
2.7	7.7	0.46
3.0	5.7	0.34

Table 1: Equivalence between pseudorapidity, η , polar angle, θ, and radial position at the front face of the ECAl endcaps.

1.1.1 Tracker

The innermost of the layers is the silicon tracker, designed to record the positions of charged particles at a number of points close to the collision vertex. This enables the reconstruction of particle tracks and, knowing the magnetic field, for their momenta to be calculated. The tracker is constructed from 13 layers in the barrel section and 14 layers in each endcap. The first three of these layers are assembled from a total of 66 million 100×150 μm^2 silicon pixels. The remaining layers consist of a further 9.6 million 180 μm wide silicon strips, ranging in length from 10 cm to 25 cm.

1.1.2 Electromagnetic Calorimeter

The second layer of the detector is the electromagnetic calorimeter. It is designed to stop and contain electrons and photons and measure their energy. It is constructed from 75,848 dense (8.2 g cm^{-3}) but optically pure Lead Tungstate crystals. These crystals form a fast homogeneous scintillator in the 420 nm range where 80% of the light is produced within 25 ns. Scintillation light from the barrel section is detected by Avalanche Photodiodes and by Vacuum Phototriodes in the endcaps. The photo-detectors are mounted on the rear of the crystals. This paper will focus on the Electromagnetic Calorimeter Endcap. The endcap detector can be seen on the right of Figure 4. A schematic of the Electromagnetic Calorimeter is shown in Figure 5 with one of the two 'Dees' that form the endcap. Most of the $PbWO_4$ crystals are grouped in 5×5 arrays called supercrystals (SCs), also shown to the right. The Dees subtend a region in pseudorapidity from 1.48 at the outside to 3.0 at the inside.

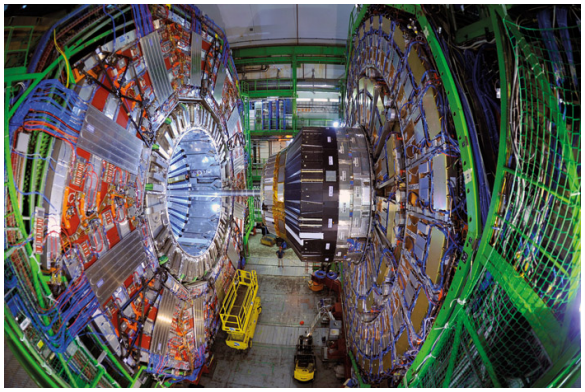

Figure 4: CMS detector barrel (left) and endcap (centre). Endcap electromagnetic calorimeter in front of the black housing.

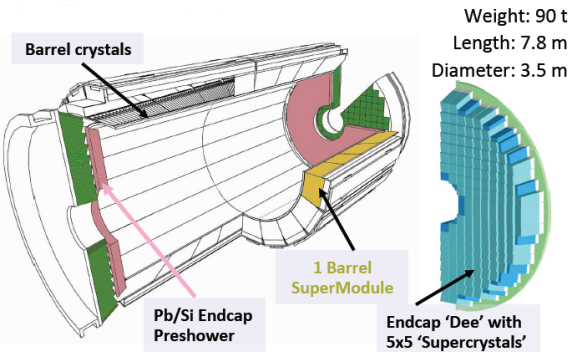

Figure 5: CMS electromagnetic calorimeter diagram (left) showing the super module structure of the barrel section. Supercrystal structure of an endcap Dee shown separately (right).

1.1.3 Hadronic Calorimeter

Following the electromagnetic calorimeter is the hadronic calorimeter which measures the energy of charged and neutral hadrons such as neutrons, protons and π mesons. The calorimeter consists of layers of brass and steel interleaved with plastic scintillators. Scintillation photons are read out by wavelength shifting fibres and finally amplified and detected by hybrid photodiodes. In the endcap high pseudorapidity range of $3.0 < |\eta| < 5.0$ the Hadronic Forward (HF) detector uses steel absorbers instrumented with quartz fibres, in which Cerenkov radiation may be produced, to measure particles in this highly irradiated region. The HF is also used to measure the instantaneous luminosity of the colliding proton beams.

1.1.4 Magnet

The fourth layer of the detector is the 3.8 Tesla superconducting solenoid magnet. It is 13 m long, 6 m in diameter and is constructed from superconducting niobium titanium coils. Although the magnet has been operated at 4 Tesla it is currently run at 3.8 Tesla in order to prolong its operational lifetime. In order to produce a magnetic field of 3.8 Tesla it operates at a current of 18,160 A and contains a total of 2.3 GJ of energy (equivalent to approximately half a tonne of TNT).

1.1.5 Muon Detector and Return Yoke

Finally the muon detector and iron magnetic field return yoke form the outermost layer. Although muons are charged they are significantly more massive than electrons. As a consequence they are far less likely to lose energy by bremsstrahlung radiation in the calorimeters and therefore pass through the inner detectors. The muon detector comprises of 3 subdetectors, all of which are gaseous in design, drift tubes (DT), cathode strip chambers (CSC) and resistive plate chambers (RPC).

Drift tubes consist of a wire housed within a 4 cm wide tube filled with an Argon/CO_2 mix and are used to measure the muons momentum in the barrel section of the detector. As a muon passes through the tube it liberates electrons from the gas which then accelerate towards the wire and are then measured. By measuring the position where the electron contacts the wire and the time taken for the electron to be seen by the wire, two of the muons co-ordinates can be determined. The DT chambers are split into layers forming a grid which allows the position and momentum of the muon to be precisely determined.

The CSCs are similar to the DTs but instead use a perpendicular grid of anode wires and cathode copper strips in chambers filled with an Argon, CO_2 and CF_4 mix to measure the momentum of muons over the endcap region. As the muon liberates electrons from the gas the electrons travel to the anode wires whilst the positively charged ions travel to the copper cathodes. These tightly packaged wires and strips are able to measure high rates of muons and their momenta, an essential characteristic in the crowded, high particle density, endcap sections.

The RPCs are used to give a fast measurement of muon momentum as input to the muon trigger. Again gaseous in design, highly resistive plastic anode and cathode plates are separated and the space between them filled with

a mixture of $C_2H_2F_4$, iC_4H_{10} and SF_6 gases. The electrons liberated by the traversing muons produce further electrons as they are accelerated by the electric field and and are collected on the electrodes where an induced charge is detected by external metal strips.

The layers of the muon detector are located between the layers of the iron return yoke. The return yoke contains the magnetic field lines generated by the superconducting magnet.

1.2 Lead Tungstate Crystals

The ECAL crystals are grown from a $50\% - 50\%$ mix of Lead Oxide (PbO) and Tungsten Oxide (WO_3). Geometrically the endcap crystals are 220 mm in length, with front and rear cross sections of 28.62x28.62 mm^2 and 30x30 mm^2 respectively [1].

Cascades of showering charged particles such as electrons and positrons are created in the crystals from the incoming high energy electrons and photons. The charged particles lose energy by ionising the crystal lattice which causes the crystals to scintillate. The scintillation light is then detected by the phototriodes. This also gives rise to an ionising radiation load on the crystals. Ionisation is also caused by the passage of charged hadrons such as charged pions.

There are two mechanisms by which the crystals lose transparency resulting in the loss of light yield. The first is through the creation of colour centres within the lattice due to the ionising radiation load, known as the dE/dx transmission response loss. This mechanism is reversible under room temperature annealing but this slower process occurs on time scales of the order of days. This annealing is seen during LHC shutdown periods. Saturation of dose rate colour centres eventually occurs at sufficiently high LHC luminosities [2].

More significant damage is caused to the crystals when direct collisions with nuclei, from high energy hadrons ($\sim$1 GeV), cause the nuclei to fission into multiple highly charged particles. These highly ionising fragments then propagate through the crystal for several microns disturbing the crystal lattice creating permanent colour centres and consequent transmission loss. This mechanism will eventually be responsible for the complete loss of light transmission [3]. The damage has been shown to be permanent at room temperature and requires annealing at 300 ^{0}C to be reversed. Heating crystals to 300 ^{0}C would require disassembly which is impractical and carries an inherent risk of inflicting damage to detector components [4].

1.3 Vacuum Phototriodes

The VPTs are 26.5 mm in diameter and are constructed from a photo-cathode deposited on the inner front surface, which is held at ground potential. A mesh anode, with 50% transparency to photo-electrons, is mounted 4.5 mm from the cathode and a dynode is mounted a further 2.5 mm rearward, as shown in Figure 6. The anode is held at +800 V and the dynode at +600 V. The photo-electrons reaching the dynode through the anode cause secondary electrons to be emitted, with a gain of $\sim$20. Half of these are then collected as a signal from the anode.

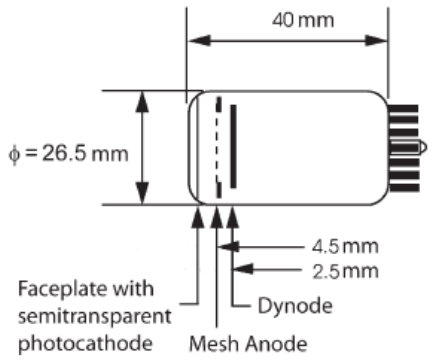

Figure 6: VPT cross section diagram [5].

'Conditioning' losses in the VPTs occur due to residual gases inside the VPT. These gases can become ionised, due to collisions with the accelerated photo-electrons and secondary electrons. The ionised gases are accelerated to the photo-cathode and the subsequent collision with the photo-cathode degrades the Caesium and Antimony coating

of the photo-cathode. This reduces the quantum efficiency of the cathode and consequently the VPTs performance. With time all the air molecules become ionised and are absorbed by the photo-cathode. The losses eventually reach an asymptotic level [6]. This mechanism exhibits room temperature annealing at approximately 10% per annum [7].

In addition, the 1.1 mm thick Borosilicate glass faceplate undergoes some transparency loss ($\sim$ 10%) due to irradiation. This loss is less than that for VPT conditioning but does not anneal [8].

1.4 High Voltage Distribution

The high voltage distribution to the VPTs is split into an upper and lower 'quadrant' on each Dee. A quadrant contains 6 or 7 high voltage 'zones' with each zone containing 12 SCs.

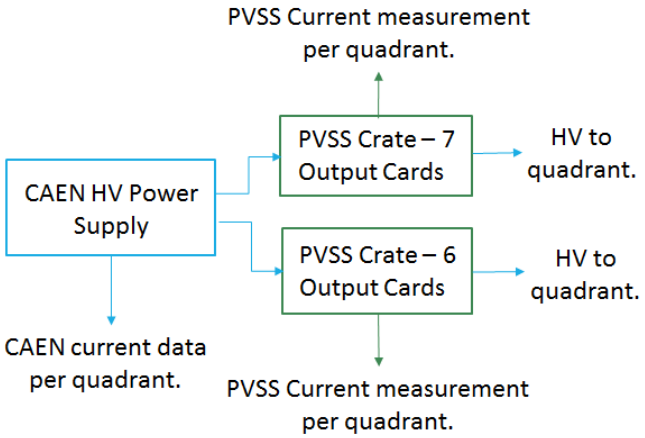

Figure 7: Diagram of the high voltage power supply system and current measurement points for the ECAL endcaps.

As shown in Figure 7, the voltages for the VPTs are delivered from a Costruzioni Apparecchiature Elettroniche Nucleari (CAEN) High Voltage power supply which feeds into the input cards of the distribution crates. These input cards measure the currents passed to the 6 or 7 output cards serving the detector zones. It is at this point that the Embedded Local Monitor Board (ELMB) measures, on a much finer scale, the current which is then recorded by the Prozessvisualisierung-und-steuerungssystem fur technische Prozesse und Ablufe (PVSS) system.

1.5 Data for Analysis

This analysis concerns 7 LHC fills throughout 2011 and 2012. The fill numbers and dates of each fill are given in Table 2. Unfortunately, due to system difficulties, the PVSS measurements were unavailable for a large portion of 2011. Due to the small signal and short fills of early 2011 the three most significant fills from this period are analysed. During 2010 the measurements were not sufficiently above the inherent noise of the system to be useful.

Month Year	Start Date	Start Unix Time (s)	Finish Unix Time (s)	Fill Number
Apr 11	28/4/11	1304015500	1304062200	1745
Apr 11	30/4/11	1304159500	1304216500	1749
May 11	2/5/11	1304305600	1304327500	1755
Apr 12	14/4/12	1334362200	1334394400	2513
May 12	2/6/12	1338610200	1338686500	2692
Aug 12	3/8/12	1343974500	1344006500	2908
Nov 12	30/11/12	1354234850	1354266400	3347

Table 2: Fill dates and details.

The luminosity, PVSS and CAEN currents were all measured from different computer systems. It was therefore necessary to align the Unix times of these measurements as they are not necessarily taken from the same time zone nor do they all necessarily take into account daylight saving hours.

The PVSS channels that take the measurements from each quadrant are referred to as EE Plus (EEP) and EE Minus (EEM), referring to the pair of Dees at the plus and minus end of the detector. The PVSS channel number refers to a single quadrant on that endcap. The CAEN channels are referred to as Dee 1, 2, 3 or 4, Ch 1 or 2 for the quadrants on each Dee.

1.6 LHC Luminosity Measurements

During operation the amplification of photo-electrons in the VPTs causes a current to be drawn from the CAEN power supply. The higher the instantaneous luminosity, the higher the current being drawn from the CAEN power supplies. This means, in order to conduct our analysis, we must normalise the VPT currents to the luminosity.

Instantaneous luminosity data is stored on the CMS Web Based Monitor (CMSWBM) and the measurements are made by the Beam Radiation Instrumentation and Luminosity (BRIL) group within CMS.

2 Measuring PVSS and CAEN Anode Currents

As described in Sections 1.4 and 1.6, the VPTs draw a current from the high voltage CAEN power supplies during running. Measurements of these currents are made both directly from the CAEN power supplies or from the high voltage input cards by the PVSS system. Both measurements consist of a signal and a baseline current, the baseline must first be removed to allow for further analysis.

2.1 PVSS Current Measurements

The PVSS anode currents are first corrected by subtracting the standing current outside the LHC fill from the measurements taken during the fill. The level outside of the fill is defined as the baseline. PVSS current measurements are recorded with a precision of 10 nA. However, the PVSS system only records data when the readings change by more than 80 nA. In addition, the noise in the system, which is approximately 100 nA, limits our resolution. The PVSS measurements of the final 9 fills of 2012 for the 4 channels of the EEP are shown in Figure 8 as a function of Unix time. The baseline currents for each channel can also be seen. The baseline for the same period is shown in more detail in Figure 9. The baselines must be subtracted from the data before further analysis. The baseline data distribution is fitted as shown in Figure 10. The mean and sigma values of the fits are taken to be the baseline value and baseline uncertainty and are listed in Table 3.

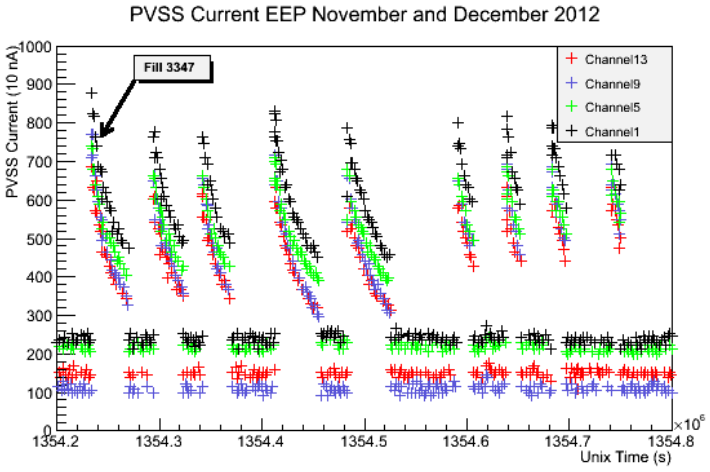

Figure 8: The current drawn by several EEP PVSS channels during November and December 2012. Each count is 10 nA.

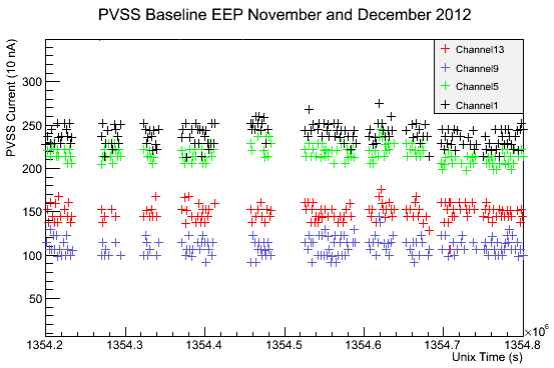

Figure 9: EEP PVSS baseline data during November and December 2012. Each Count is 10 nA.

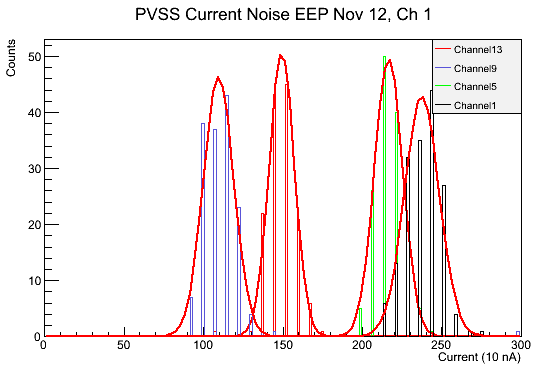

Figure 10: Observations of baselines for EEP PVSS channels during November 2012. Each count is 10 nA.

During 2011 the EEM channels were stable whilst the EEP measurements were not. The only instability during 2012 was in EEM Ch-1 during Nov 2012. A large rise in baseline was observed due to a VPT short circuit. However the baseline after the sudden increase was stable. The VPT short inadvertantly provided an additional and useful check for the current scale of the system.

Due to the system difficulties in 2011 the EEP Apr 2011 baselines were continually rising with time. As a consequence, baseline measurements were only taken close to the fill concerned in order to minimise the effects of this problem. In addition, due to the low luminosities at the start of 2011 only data after the 28^{th} of April have been used.

PVSS EEP Nov 2012 Baselines (μA)			
EEP - Ch1	EEP - Ch5	EEP - Ch9	EEP - Ch13
2.38 ± 0.11	2.17 ± 0.9	1.10 ± 0.10	1.50 ± 0.8

Table 3: Measurement of baselines for EEP PVSS channels during November 2012.

2.2 CAEN Anode Current Measurements

CAEN anode currents can either be taken from the CMSWBM database or directly from the CAEN power supply display window, as shown in Figure 11. The measurement precision for the CAEN currents is 500 nA and the database is updated when a current change of greater than 500 nA takes place. During operation the VPT dynodes supply a negative current to the CAEN power supplies, therefore a standing current offset of at least 200 μA is needed to counter these effects.

28 Aug 2012, 15.40
EE+ CAEN settings, no beams

davec@srv-c2c04-22:~

- Main Utility Setup Groups View User

Group 00

Channel Name	V0Set	I0Set	VMon	IMon	Pw	Status	Ch#
Anode__+NQL	800.0 V	475.0 uA	799.3 V	364.0 uA	On		06.0000
Dynode_+NQL	600.0 V	375.0 uA	599.5 V	273.0 uA	On		06.0001
Anode__+NQU	800.0 V	475.0 uA	799.5 V	364.5 uA	On		06.0002
Dynode_+NQU	600.0 V	375.0 uA	599.5 V	272.0 uA	On		06.0003
Test	800.0 V	475.0 uA	0.6 V	0.0 uA	Off		06.0004
Test	600.0 V	375.0 uA	0.4 V	0.0 uA	Off		06.0005
SN0497CH006	0.0 V	0.0 uA	0.0 V	0.0 uA	Off		06.0006
SN0497CH007	0.0 V	0.0 uA	0.0 V	0.0 uA	Off		06.0007
SN0497CH008	0.0 V	0.0 uA	0.1 V	0.0 uA	Off		06.0008
SN0497CH009	0.0 V	0.0 uA	0.1 V	0.0 uA	Off		06.0009
SN0497CH010	0.0 V	0.0 uA	0.0 V	0.0 uA	Off		06.0010
SN0497CH011	0.0 V	0.0 uA	0.0 V	0.0 uA	Off		06.0011
Anode__+FQU	800.0 V	475.0 uA	800.0 V	363.5 uA	On		09.0000
Dynode_+FQU	600.0 V	375.0 uA	599.9 V	273.5 uA	On		09.0001
Anode__+FQL	800.0 V	475.0 uA	799.7 V	365.5 uA	On		09.0002
Dynode_+FQL	600.0 V	375.0 uA	599.8 V	273.0 uA	On		09.0003
Test__Anode	0.0 V	10.0 uA	0.1 V	0.0 uA	Off		09.0004
Test_Dynode	0.0 V	10.0 uA	0.3 V	0.0 uA	Off		09.0005
SN0515CH006	0.0 V	0.0 uA	0.3 V	0.0 uA	Off		09.0006

Channels Display/Edit Screen LocEn V0 I0 T CAEN SY1527

Figure 11: CAEN power supply readout screen shot, EEP August 28^{th} 2012. The IMon column shows the anode and dynode current baseline measurements under zero beam conditions for the two quadrants on each of the two Dees.

Readings from the power supply screen under zero beam conditions are available for the 7^{th} February and 28^{th} August 2012. Data from the CAEN screens agree to within 0.5 μA to that recorded by the CMSWBM system.

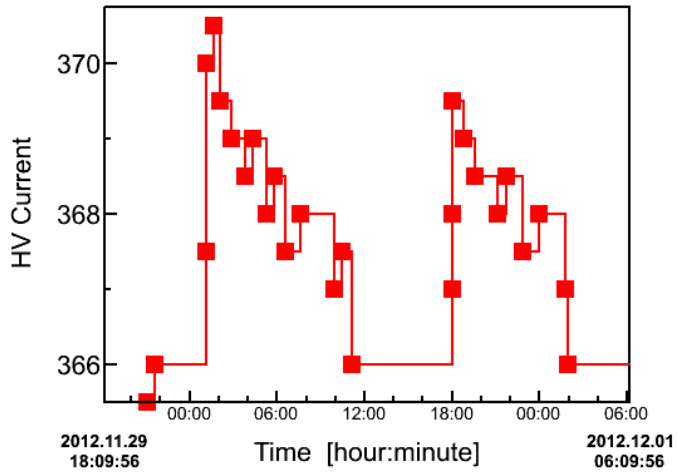

Figure 12: CMSWBM CAEN readout for Dee 1 Ch 2 in Nov 2012 for 2 LHC fills. The vertical axis represents the total CAEN current in μA

.

Two fills, recorded by the CMSWBM systems at the LHC, are shown in Figure 12. The baseline taken outside of the fills is 366 μA. For the first fill the peak net current is 370.5 μA. This yields an LHC current of 4.5 μA.

3 PVSS and CAEN Channel Correspondence Checks

Whilst the CAEN measurements are direct readings of anode current, the PVSS measurements are recorded in number of counts. In order to verify the expected 10 nA/count we must compare the output of each PVSS channel to the corresponding CAEN channel.

In order to perform this check, each PVSS must be correctly matched to the corresponding CAEN channel. Each Dee contains one quadrant with 6 zones and one quadrant with 7 zones. After subtracting the baselines, the

additional 6^{th} of current should be clear to see and an association can be made.

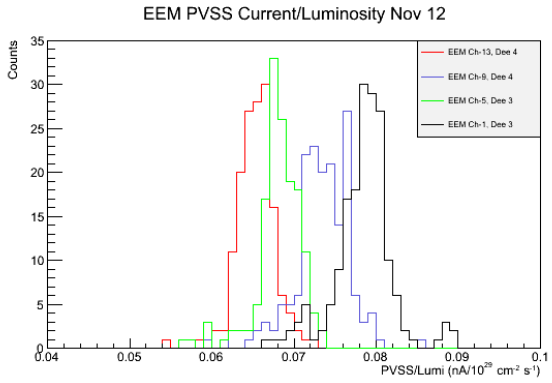

Figure 13: PVSS currents over instantaneous luminosity against Unix time for EEM Nov 2012.

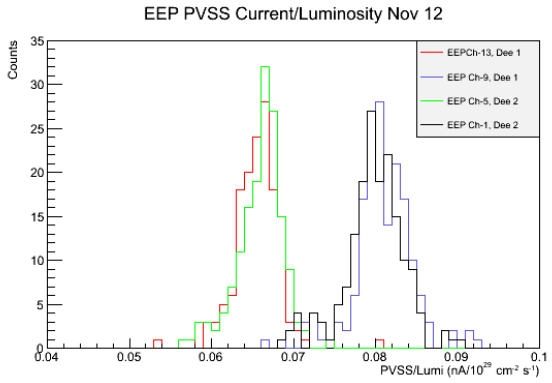

Figure 14: PVSS currents over instantaneous luminosity against Unix time for EEP Nov 2012.

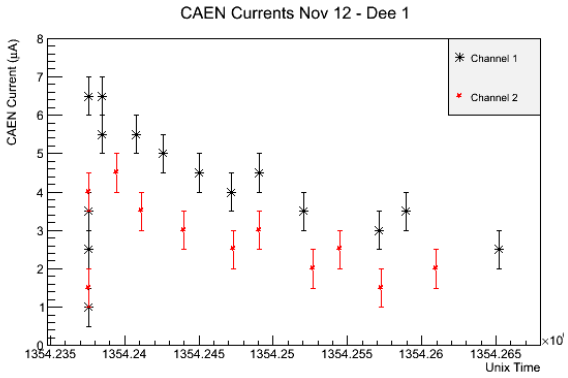

Figure 15: CAEN currents for Dee 1 Ch-1 and Dee 1 Ch-2 against Unix time, Nov 2012.

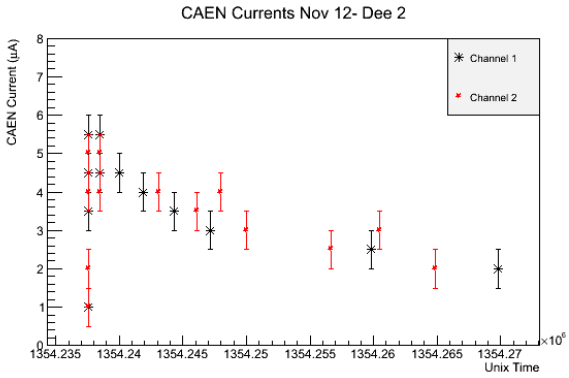

Figure 16: CAEN currents for Dee 2 Ch-1 and Dee 2 Ch-2 against Unix time, Nov 2012.

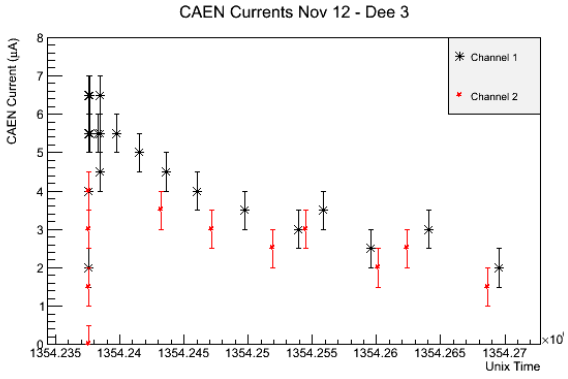

Figure 17: CAEN currents for Dee 3 Ch-1 and Dee 3 Ch-2 against Unix time, Nov 2012.

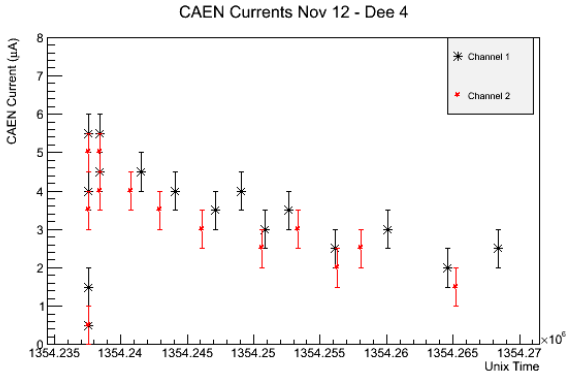

Figure 18: CAEN currents for Dee 4 Ch-1 and Dee 4 Ch-2 against Unix time, Nov 2012.

Figures 13 and 14 show the PVSS current to luminosity ratio for the four quadrants on each endcap against Unix time for fill 3347. We see a clear distinction between the channels with 6 or 7 zones. Channels 1 and 9, shown in black and blue, demonstrate a significantly higher PVSS to instantaneous luminosity ratio compared to that of Channels 5 and 13, shown in green and red. This distinction is not as clear for EEM, as Channel 9 appears slightly lower than expected. The reason for this is currently unknown but the difference in currents between quadrants with 6 or 7 zones is deemed to be significant enough to make the necessary distinction.

Figures 15 - 18 show the CAEN currents measured for fill 3347 as a function of Unix time. The currents in Figures 15, 17 and 18 show additional currents of between 0.5 and 1 μA for Channel 1 (black data points) compared to the red data of Channel 2. However, the CAEN data for Dee 2 in Figure 16 do not show the expected differences in

current. The cause for this unexpected similarity in currents is presently unknown. Therefore the Channel numbers for Dee 2 in the left hand column of Table 4 are not defined.

The concluding correspondencies between CAEN and PVSS channels are given in Table 4. F or N refers to the Dees nearest or farthest from the centre of the LHC. + or - refers to the Dees at the plus or minus end of the detector. Finally, U or L refers to the upper or lower quadrant of each Dee.

CMSWBM CAEN Channel	ELMB CAEN Channel	PVSS Channel	N^o of Zones
Dee 1 Ch-1	+FQU	EEP Ch-9	7
Dee 1 Ch-2	+FQL	EEP Ch-13	6
Dee 2 Ch-1 or 2	+NQL	EEP Ch-1	7
Dee 2 Ch-1 or 2	+NQU	EEP Ch-5	6
Dee 3 Ch-1	-NQU	EEM Ch-1	7
Dee 3 Ch-2	-NQL	EEM Ch-5	6
Dee 4 Ch-1	-FQL	EEM Ch-9	7
Dee 4 Ch-2	-FQU	EEM Ch-13	6

Table 4: Correspondence between PVSS and CAEN channels.

4 PVSS and CAEN Agreement

The PVSS data has a much better resolution and frequency of measurement than the CAEN data. As a consequence the PVSS data will be used as the main current measurement for the rest of this paper. The CAEN currents are taken as the absolute reference. PVSS currents are checked against the CAEN currents by comparing the measurements taken during LHC fill 3347 in November 2012, as shown in Figure 19. A Chi squared is calculated from the difference between the PVSS and CAEN currents. The PVSS scale is then adjusted to minimise the value of Chi2 for each channel. One example of this minimisation technique is shown in Figure 20, where the best agreement is found to be at an adjustment factor of $\times 0.95$.

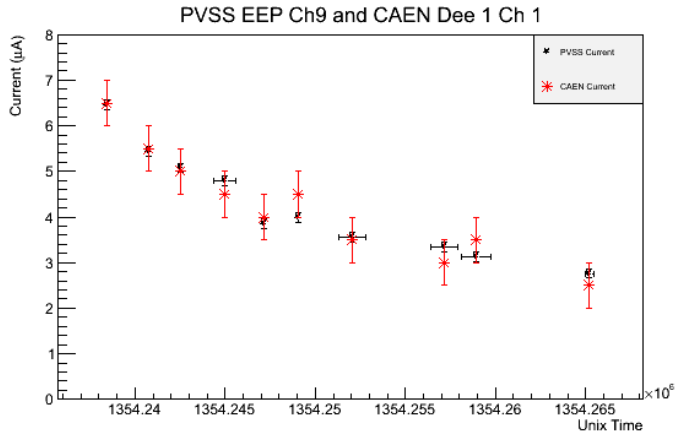

Figure 19: PVSS EEP Ch-9 and CAEN Dee 1 Ch-1 currents during fill 3347 in Nov 2012.

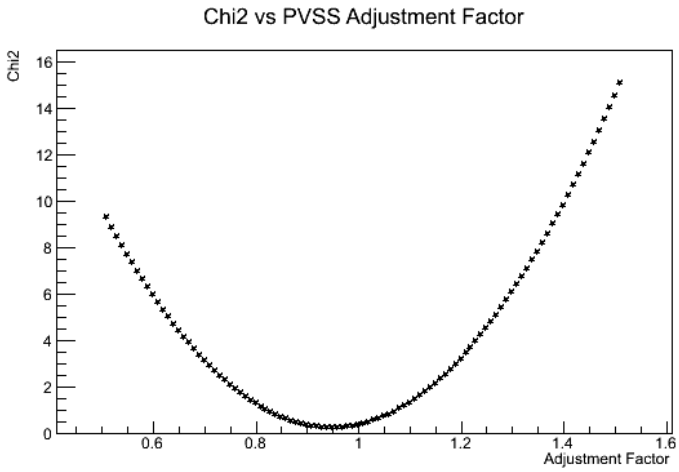

Figure 20: The PVSS adjustment factors against Chi2 from fill 3347 in Nov 2012 for PVSS EEP Ch-9 compared to CAEN Dee 1 Ch-1.

The CAEN and PVSS measurements were not taken at identical times. Therefore the PVSS measurement with the closest Unix time to the CAEN measurement was assigned to that data point, due to the higher frequency of PVSS data taking. If a PVSS data point could not be found within 30 minutes of the CAEN data, the data point was discarded. However, the majority of measurements fell well within this time frame.

CAEN Channel	PVSS Channel	Scaling Factor (CAEN/PVSS)
Dee 1 Ch-1	EEP Ch-9	0.95
Dee 1 Ch-2	EEP Ch-13	0.8
Dee 3 Ch-1	EEM Ch-1	1.06
Dee 3 Ch-2	EEM Ch-5	0.94
Dee 4 Ch-1	EEM Ch-9	1.07
Dee 4 Ch-2	EEM Ch-13	1.02

Table 5: PVSS to CAEN scaling factors.

Table 5 shows the scaling factors that minimise the Chi2 between corresponding PVSS and CAEN channels for fill 3347 in November 2012. The average scaling factor is 0.97 with an RMS spread is 9%. Therefore PVSS and CAEN current measurements are considered to be in agreement. The CAEN data for Dee 1 Ch-2 appear to be low, giving a scaling factor of only 0.8. This may be due to noise and the difficulty in establishing the CAEN baseline to better than 0.5 μA. Due to the CAEN identification problems, the Dee 2 channels were not analysed. For the rest of this paper a single PVSS count is taken to be 10 nA, with the relation between PVSS and CAEN current taken to be unity.

5 Luminosity Fitting

The PVSS currents are not taken at prescribed times. In order to compare the PVSS currents to the LHC instantaneous luminosity in CMS, fits are made separately to the luminosity and PVSS data with respect to time. The fits are used to establish the dependence of the PVSS current data as a function of luminosity.

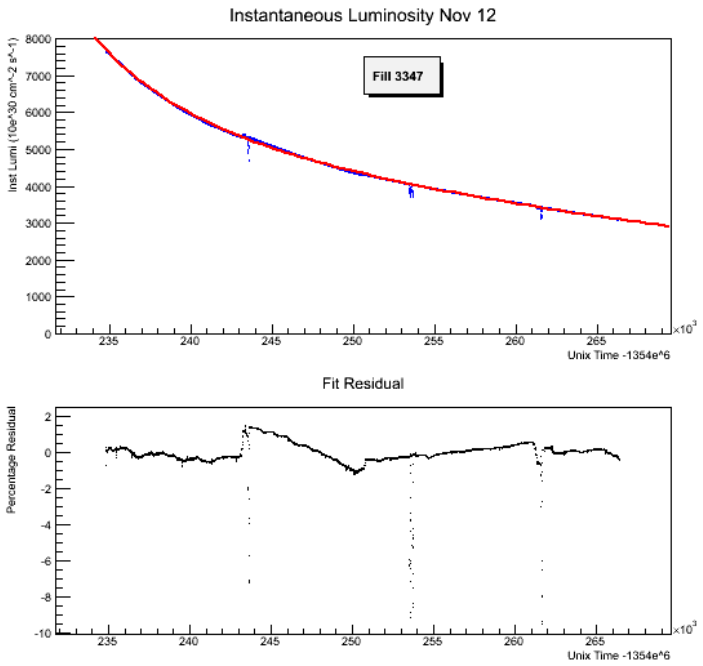

Figure 21: Top, instantaneous luminosity measurements as a function of Unix time and, bottom, the fit residual for fill 3347 in Nov 2012. The duration of the fill is 8 hours.

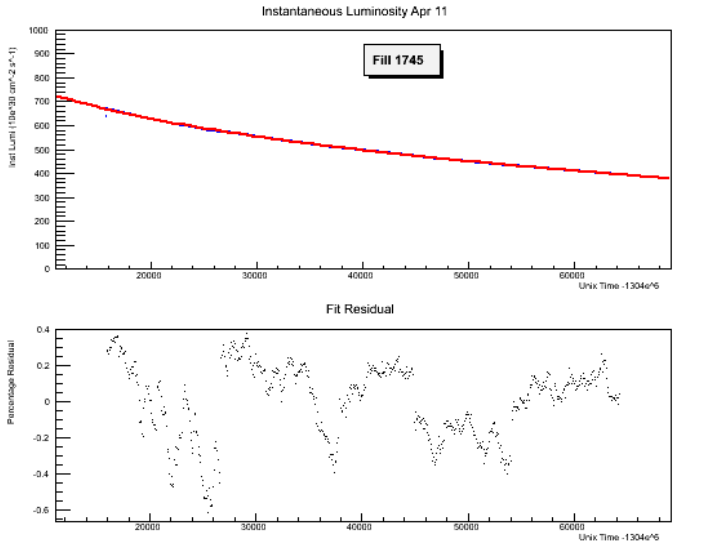

Figure 22: Top, instantaneous luminosity measurements as a function of Unix time and, bottom, the fit residual for fill 1745 in Apr 2011. The duration of the fill is 14 hours.

Figure 21, top, shows a double exponential fit to the luminosity data from fill 3347 in Nov 2012 as a function of Unix time. The percentage residuals to the fit are shown in Figure 21 bottom. 99.4% of the data falls within $\pm 1.6\%$ of the fit. The very brief drops in luminosity, at 244, 254 and 262 on the x axis, originate from the Van der Meer scans used to test beam alignment. Longer excursions of the residual are believed to be corrections to the beam steering to achieve higher luminosities. However, the level of the residuals are well within the precision needed for the studies of this paper. In contrast, Figure 22 shows the instantaneous luminosity and residuals of fill 1745 in April 2011 where the residuals are all within $\pm$ 0.6$\%$.

These examples also show the increase in luminosity from April 2011 to November 2012. The April 2011 luminosity is approximately ten times lower than that for November 2012, which gives rise to worse signal to noise

ratio from the PVSS system in 2011 than in 2012.

6 PVSS Fitting

It is expected that the current drawn by the detector is directly proportional to the luminosity. As a consequence, double exponential fits are also applied to the PVSS data.

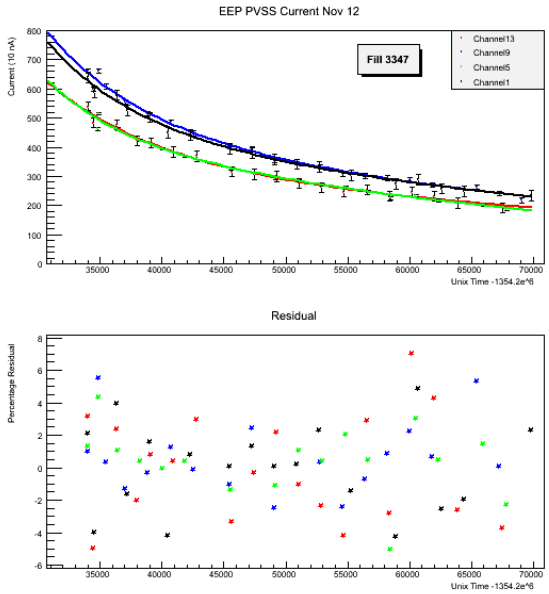

Figure 23: PVSS current measurements and fit residual for fill 3347 in Nov 2012 as a function of Unix time.

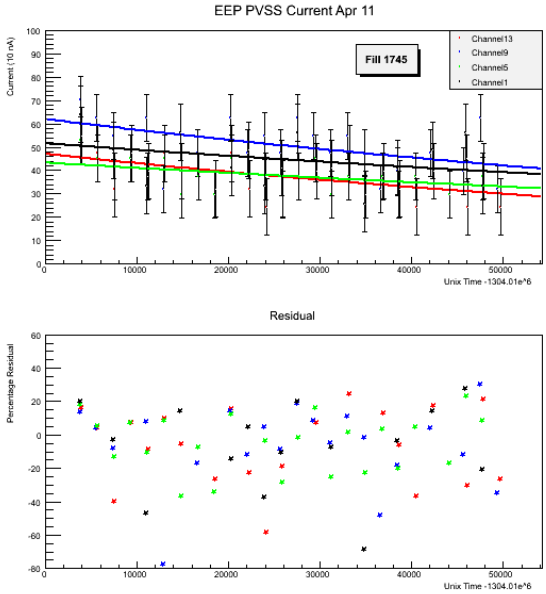

Figure 24: PVSS current measurements and fit residual for fill 1475 in Apr 2011 as a function of Unix time.

As shown in Figure 23, the double exponential fits describe the high intensity fills, generating anode currents of $\sim$6.5 μA, of November 2012 well. However, the ROOT minimisation techniques struggle with the low intensity fills, with currents of $\sim$0.7 μA in 2011. The lower luminosities in this period generate significantly lower currents, resulting in a larger noise to signal ratios, as shown in Figure 24. This sometimes gives rise to nonsensical fit parameters and excessive error estimates. For this reason we have fitted both single and double exponentials to all the fills used in the analysis and evaluated the behaviour and goodness of each fit in order to decide which fit to take forward to further analysis. The lower signal to noise ratio results in percentage residuals approximately ten times larger in fill 1745 compared to those in fill 3347.

7 VPT Response

As previously explained in Section 1.3, VPTs lose response through conditioning and faceplate darkening. The analysis of these losses in CMS is discussed in detail in Sections 11 and 12. In order to estimate the VPT conditioning losses the integrated photo-cathode current in each VPT must be evaluated. However, only VPT anode currents, not VPT photo-cathode currents, are available. These are at the quadrant level (1831 VPTs) and Dee level (3662 VPTs). To estimate the photo-current drawn by each VPT, a sum is made over all VPTs on a Dee, folded with the radiation field and laboratory characteristics of each VPT. From this, a quality factor (Q Factor) for each VPT can be calculated, see Equation 2. The normalised PVSS anode current per unit of instantaneous luminosity is proportional to the integrated Q factor for each Dee as shown in Equation 3.

The instantaneous photo-cathode current for any particular VPT can be calculated using Equation 4. The photo-cathode current is calculated from the anode current expected for the VPT divided by the DC gain at 0 Tesla provided by the manufacturer. This can then be used to evaluate the integrated cathode currents from the start of LHC running.

$$\text{Q Factor} = \text{Quantum Efficiency} \times \text{Gain} \times \text{Radiation Field} \times \text{Magnetic Field Adjustment} \times \text{Crystal Light Yield} \quad (2)$$

$$\alpha \times \text{Q Factor}_{Dee} = \frac{\text{PVSS Anode-Current}}{\text{Instantaneous Luminosity}} \tag{3}$$

$$\text{VPT Cathode Current} = \frac{\alpha \times \text{Q Factor}_{VPT} \times \text{Instantaneous Luminosity}}{\text{Gain}} \tag{4}$$

7.1 VPT Quantum Efficiency and Gain

The Q factor depends on the VPT quantum efficiency and gain, both of which were measured under zero magnetic field by the manufacturer, Research Institute Electron (RIE), St Petersburg, Russia. The VPTs were then delivered to the Rutherford Appleton Laboratory (RAL) where they were tested under a 1.8 T magnetic field. These tests allowed the VPTs to be benchmarked against each other. About 10% of VPTs were also tested at Brunel University under a 4 T field. All VPTs were again tested at 0 T once delivered to CERN to ensure they were transported safely.

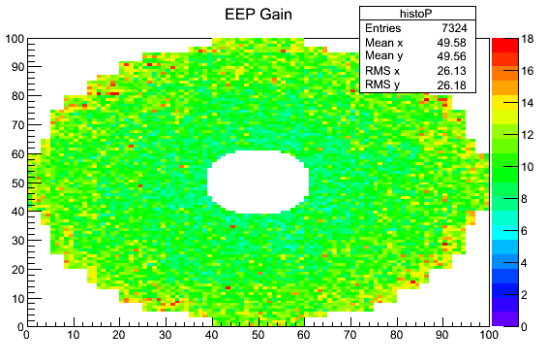

Figure 25: EEP VPT DC gain at 0 Tesla.

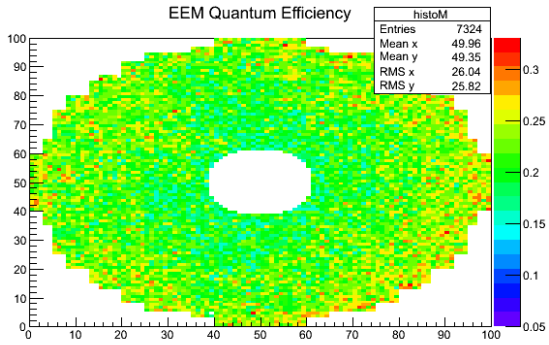

Figure 26: EEM VPT quantum efficiency at 0 Tesla.

Figures 25 and 26 show the EEP VPT DC gains and EEM VPT quantum efficiencies measured at 0 Tesla by the manufacturer. The VPT values are shown on the right hand scale of the plots. The VPTs are on an X-Y grid indicating their position on the Dee. The average quantum efficiency is 20% whilst the average DC gain is 10.1.

During assembly VPTs were arranged so that those with the highest electron/MeV yield were positioned outer most, with the lowest yielding VPTs at the centre. The VPTs were arranged in this way since higher energy particles pass through the detector at larger pseudo-rapidity, where higher channel noise is acceptable.

7.2 Crystal Light Yield

The light yield of the crystal determines the number of scintillation photons that reach the VPT cathode, therefore influencing the generation of the photo-current. The crystals were manufactured at two different locations and with two different methods meaning each set possess slightly different properties.

The majority of crystals (∼12,500) were produced at Bogoroditsk Techo Chemical Production (BTCP), Russia. Around 2,000 crystals were manufactured at the Shanghai Institute of Ceramics (SIC), China. The Chinese crystals possess higher light yield, but do not display as high a level of light yield uniformity relative to the Russian crystals. Reasons for sourcing crystals from two manufacturers include the need for higher production capacities and to avoid creating a monopoly in the business sector.

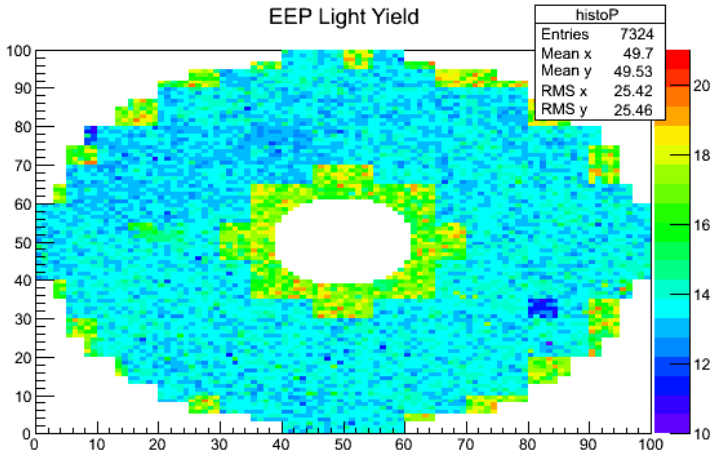

Figure 27: EEP crystal light yield. Right hand scale is in units of photons/MeV.

Due to the lower uniformity of the Chinese crystals, these were placed around the inside and outside of the detector. However, a set of Chinese crystals used at the test beam were placed in the equivalent position on Dee 4 to enable calibrations at the test beam and in situ at CMS to be compared.

All crystal light yields were tested at CERN or the University of Rome La Sapienza using a Co^{60} source. The Chinese crystals were tested for radiation hardness at SIC. An average light yield of 14.1 Photons/MeV is observed from Figure 27, for EEP. An average of 14.1 Photons/MeV was also measured for EEM.

7.3 Magnetic Field Adjustment

The production of the VPT anode current is reliant on the number of photo-electrons which are released from the photo-cathode. These electrons are accelerated towards the anode where they have a $50\% - 50\%$ chance of being collected or of passing through the mesh to the dynode. At the dynode $\sim$20 secondary electrons are produced for each photo-electron impact, which travel back to the anode, where $\sim$50% are collected. This gives rise to the net gain of the tube.

Electrons travelling at an angle to the mesh no longer see the $50\% - 50\%$ split of mesh and vacuum due to the 3D nature of the anode, thus affecting gain. The strength and angle of the magnetic field in CMS, relative to the VPT axis, determine the number of secondary electrons from the dynode which are collected by the anode. Coupled with the VPT electric field it affects the direction and radius of the electron spirals. The anode-current detected is dependent on these factors that are grouped together as a 'magnetic field adjustment' [11].

These adjustment factors have been measured as a function of the VPT location on the detector and were determined by Sasha Ledovskoy. Figure 28 shows the adjustment factors as a function of VPT position. The values are also listed in Table 15 in the appendices. The magnetic field adjustment factor ranges from 0.68 at the innermost radius to 0.83 at the outermost, with a peak of 0.85 at a radial VPT position of 0.36 with respect to the x axis, equivalent to 1.15 m.

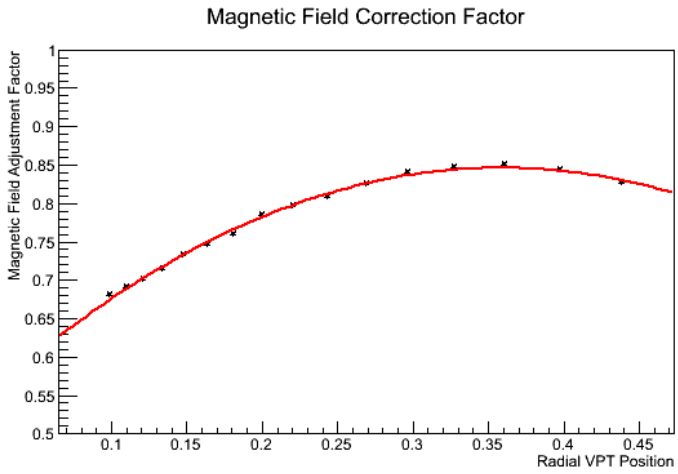

Figure 28: Magnetic field adjustment factor. The radial position is in units of the VPT X-Y grid with respect to the centre of the Dee, divided by 100 [12].

7.4 Radiation Field

The final component we require to determine the Q factor is the radiation field across the EE, since the amount of scintillation light is dependent on the level of radiation incident on the detector. The radiation as a function of radial position is shown in Figure 29 [12] and was obtained from the FLUKA simulation of the particle flux from collisions in CMS [13]. The data shows the exponential rise in the radiation field towards the centre of the detector. This is the main factor which will cause the ECAL Endcaps to significantly degrade from the innermost regions first.

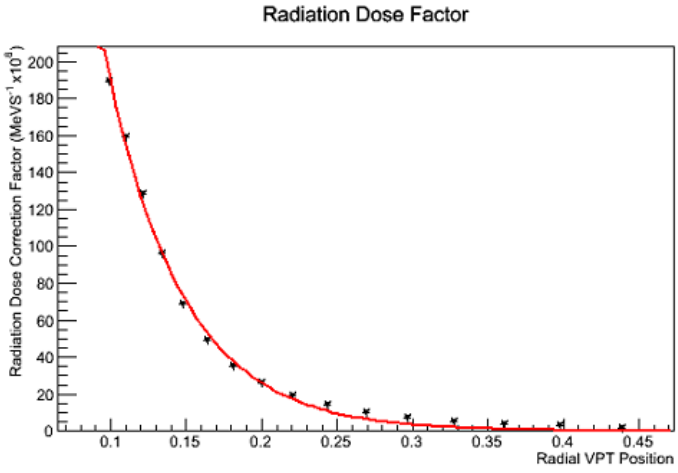

Figure 29: Energy deposited in a volume of $2.9\times2.9\times22$ cm^3 of Lead Tungstate crystal per second at an instantaneous luminosity of 1×10^{34} cm^{-1}s^{-1} for 7 TeV collisions. The radial position is in units of the VPT X-Y grid with respect to the centre of the Dee, divided by 100.

7.5 Anode Current as a Function of Radius

It is now possible to calculate the relative current that will be seen from each VPT. In order to illustrate the levels of current drawn from different pseudorapidity regions of the detector, the percentage of the total VPT current has been calculated for radial bands 4 VPTs wide, as shown in Table 6. The second and third columns show the percentage of the total current and the percentage of VPTs in each pseudorapidity band. The fourth column shows the relative importance of each VPT to the total anode current, calculated from the percentage current divided by the percentage of VPTs. The pseudorapidity range of each band is shown in the fifth column.

Band	VPT Current %	VPT %	Relative Importance	Pseudorapidity Range
1	42.7	4.8	8.89	2.79 - 3.00
2	25.8	6.3	4.11	2.54 - 2.79
3	13.2	7.4	1.78	2.35 - 2.54
4	8.0	9.1	0.89	2.18 - 2.35
5	4.7	10.4	0.45	2.04 - 2.18
6	2.6	11.5	0.23	1.92 - 2.04
7	1.5	13.4	0.12	1.82 - 1.92
8	0.8	14.5	0.06	1.72 - 1.82
9	0.5	15.4	0.03	1.64 - 1.72
10	0.1	7.3	0.02	1.56 - 1.64

Table 6: Percentage of VPT current, column 2, that originates from bands of 4 VPTs and the percentage of VPTs in these bands, column 3. Column 4, the relative importance to the total current, from each VPT. Column 5, the pseudorapidity range of each band.

As can be seen the majority of the current originates from the inner most regions of the detector with 68.5% of end cap current being delivered by the inner most 11.2% of VPTs. Comparing the ratio of VPT current to the number of VPTs between Band 1 and Band 9 we see the average VPT in Band 1 produces 270 times more current than a VPT in Band 9. This large difference in the levels of current is due to the exponential nature of the radiation field. The VPT percentage for Band 10 is lower due to the shape of the edges of the outer detector.

8 Evolution of the Normalised PVSS Current with Time

The ratios of the PVSS current to the instantaneous luminosity have been calculated from 7 fills from April 2011 to November 2012. The ratios are taken from the fits to the PVSS and luminosity data at the start and end of the fills, as shown in Figures 30 and 31.

Taking data from the beginning and end of the fills we find each of the four 2012 fills have an RMS spread for the value of PVSS current over luminosity of within 4% across all four Dees. Figure 30 shows that as running continues and the integrated luminosity rises throughout 2011 and 2012, the response of the PVSS currents relative to the instantaneous luminosity decrease. This is due to the response losses in the detector caused by the high radiation fields in the endcaps. The last fill in 2012, fill 3347, shows a normalised current that is only 46% of the normalised current in April and May 2011. The average values of PVSS to luminosity ratio for each cluster of data points in Figure 30 are given in Table 7.

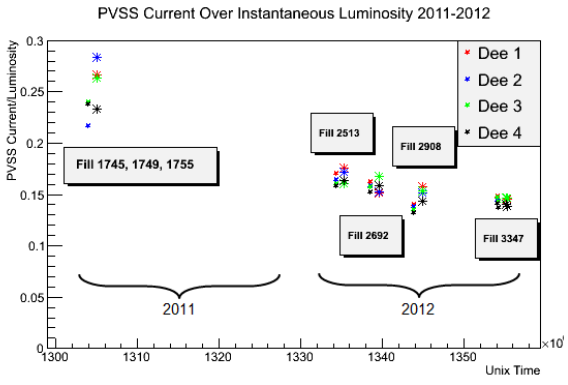

Figure 30: PVSS current over luminosity for all fills evaluated. Data points on the left of each cluster are for the 4 Dees at the start of the fill and to the right for the 4 Dees at the end of the fill.

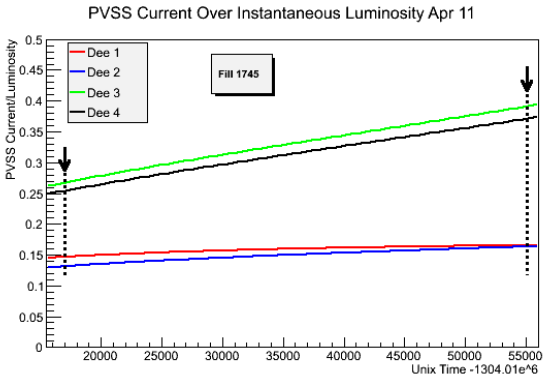

Figure 31: Fits for PVSS current over luminosity for for fill 1745 in April 20ll. The arrows indicate the start and finish of the fill.

Month - Year	Average Value
April/May - 2011	0.247
April - 2012	0.169
August - 2012	0.156
September - 2012	0.145
November - 2012	0.144

Table 7: Average value of PVSS to luminosity ratio for each cluster of data points in Figure 30

.

9 Laser Monitoring System

The rear face of each crystal is mounted with a quartz fibre optic cable that delivers pulses of ∼500 nm laser light to the crystals. The light propagates to the front face of the crystal where it is internally reflected and travels to the rear of the crystal before being detected by the VPT. By pulsing laser light through the crystals during LHC operation it allows in situ calibration of the detector and measurements of total detector response to be made [1].

The laser monitoring data from the CMS ECAL is shown in Figure 32 from 2011 to 2012. The data is averaged over 5 bands of pseudorapidity. Each band is 0.3 units of pseudorapidity wide, across the endcaps. The region for $|\eta| < 1.4$ represents the barrel. The higher the value of η in the band the higher the relative response loss of the detector. This is due to the exponential decrease in radiation field with VPT radius as seen in Section 7.4, Figure 29. The instantaneous luminosity throughout 2011 and 2012 running is also shown at the bottom of Figure 32 and is a contributing factor to the rate of detector response loss, especially the dE/dx crystal transmission component.

According to the data from the laser monitoring system the detector is at approximately 95% of its original response for the innermost region of $2.7 < \eta < 3.0$ during April 2011. The relative response is reduced to 35% of the original detector response by the end of November 2012.

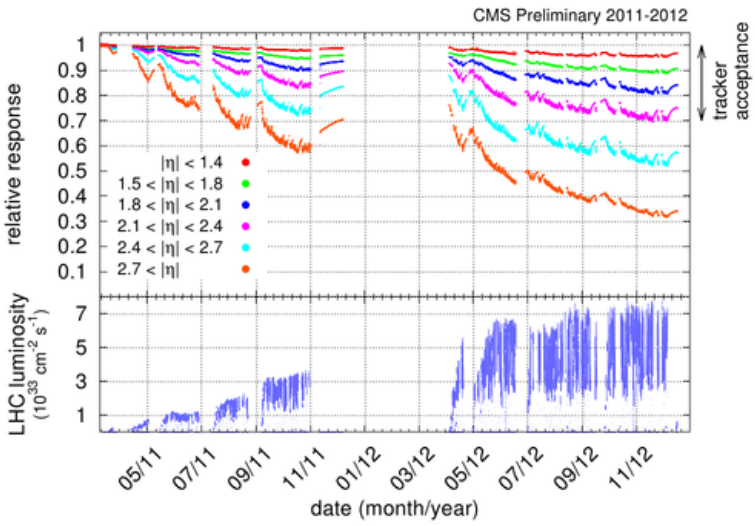

Figure 32: Relative response of ECAL laser monitoring system used to calibrate the detector throughout LHC running against time during 2011-12 [14].

A direct quantitative comparison between Figures 30 and 32 cannot be made as Figure 30 is averaged over a Dee and Figure 32 is averaged over bands of pseudorapidity. However, similar trends in both figures demonstrate a sustained and increasing level of response loss within the detector with time, providing an independent verification of such processes occurring within the detector.

10 Calculating Alpha

The normalisation co-efficient α is required to determine the VPT photo-cathode current at any given instantaneous luminosity as described in Equation 4. Alpha was calculated for the April and May 2011 fills to evaluate the behaviour of the detector as close as possible to the start of LHC operation where the crystals are expected to have undergone minimal transmission losses.

Due to the difficulty in establishing an accurate fit, which originates from the small signal for the 3 April and May 2011 fills, we have averaged the values of α from this period. These data have an RMS of 10.6%. The PVSS current to instantaneous luminosity ratio for the four Dees throughout fill 1745 in April 2011 are shown in Figure 31. The dotted lines indicate the start and end of the fill and the values used to calculate the data points for the April 2011 period in Figure 30.

Tables 8 and 9 show measurements of α, averaged over the three April and May 2011 fills, from the beginning and end of the fills and the summed Q factors for the four Dees.

Fill Start Apr/May 2011				
	Dee 1	Dee 2	Dee 3	Dee 4
PVSS/Lumi	0.237	0.216	0.239	0.238
Q Factor	755770	841980	855370	731430
α	3.14×10^{-7}	2.57×10^{-7}	2.80×10^{-7}	3.25×10^{-7}

Table 8: Normalised PVSS to luminosity data and the Q factors for the four Dees. Last row shows the resultant average value of α for the start of the three fills in April and May 2011.

Fill End Apr/May 2011				
	Dee 1	Dee 2	Dee 3	Dee 4
PVSS/Lumi	0.266	0.284	0.263	0.233
Q Factor	755770	841980	855370	731430
α	3.52×10^{-7}	3.37×10^{-7}	3.07×10^{-7}	3.19×10^{-7}

Table 9: Normalised PVSS to luminosity data and the Q factors for the four Dees. Last row shows the resultant average value of α for the end of three fills in April and May 2011.

	Fill Start	Fill End	Fill Start and End
Average α	2.94×10^{-7}	3.29×10^{-7}	3.11×10^{-7}
RMS	10.9%	7.0%	10.6%

Table 10: Average alpha results.

The spread of Q Factors across the 4 Dees has an RMS of 6.7%, as quantified in Tables 8 and 9. These differences are possibly due to variations in crystal light yields and VPT characteristics. Dee 1 is slightly lower at approximately 5% below the average. It was the first Dee to be constructed and the crystal growing processes may not have been perfected yet. Dee 4 is also lower at 8% below the average. It was the last to be constructed and may contain weaker performing crystals and VPTs.

Differences in the values of α, as shown in Tables 8 - 10, may be due to the difficulty in accurately fitting the PVSS data due to the small signal relative to the noise of the system during 2011. Due to the disparities in alpha between each Dee and at the beginning and end of each fill, an average value of α from both the start and end of each fill, of 3.11×10^{-7}, will be used for further analysis.

11 VPT Conditioning

To determine the in situ detector VPT conditioning levels we must compare the integrated VPT photo-cathode currents, calculated from Equation 4, to the observed levels of VPT conditioning, as a function of integrated photo-cathode charge, measured at the 4 Tesla test rigs at Brunel and the University of Virginia (UVa) [16]. The VPT conditioning is a combination of a fast and slow exponential decay. The double exponential fit parameters

from 26 test VPTs are shown in Figure 33. The 26 fits are averaged to produce a single fit, as shown in Figure 34, which is used to determine the in situ VPT conditioning for any given integrated cathode charge. The error bars are taken to be the RMS of the 26 individual fits for a given integrated charge. The asymptotic loss is 27% with an RMS spread of 13%. The dates at which a VPT anode current of 10 mC is expected to have been drawn for each band of 0.3 units of pseudorapidity are given in Appendix B.

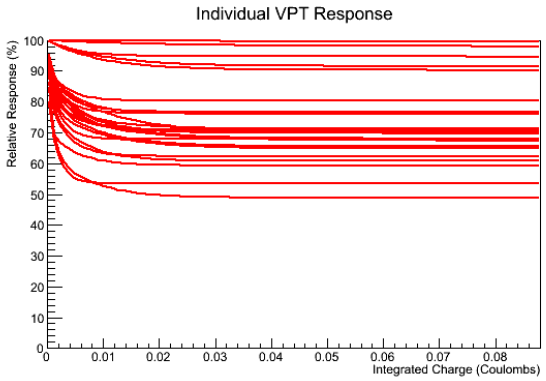

Figure 33: Relative response of 26 VPTs from Brunel and UVa 4 Tesla test rigs as a function of integrated charge taken from the photo-cathode.

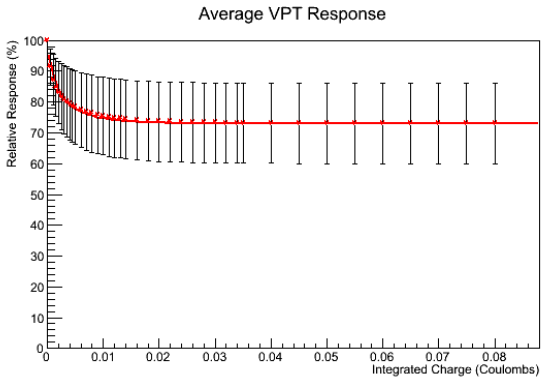

Figure 34: Average response of 26 VPTs from Brunel and UVa 4 Tesla test rigs. Error bars are the RMS values from Figure 33.

12 VPT Faceplate Transmission Losses

The VPT faceplates undergo a loss of tranmission due to colour centres created by the electromagnetic dose. Figure 35 shows the measured VPT faceplate relative transmission at $\sim$ 420 nm after irradiation with protons from the Proton Synchrotron (PS) at CERN [17]. A proton fluence of 10^{11} cm^{-2} at the PS was assumed to be equivalent to an electromagnetic dose of 20 kGray in CMS. Unlike Lead Tungstate crystals, transmission losses due to dose in the Borosilicate glass do not anneal at room temperature. The response profile shown in Figure 35 has been folded with the emission spectrum of the Lead Tungstate crystals. The figure shows a faceplate transmission of 92.8% at 20 kGray and that the transmission becomes asymptotic at 90.5% with respect to the initial transmission.

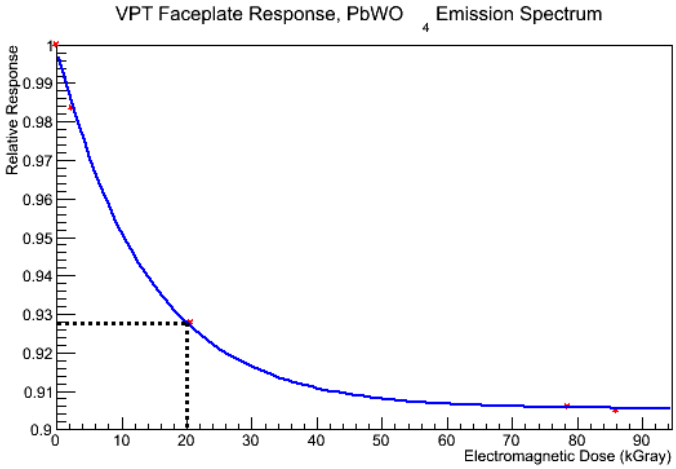

Figure 35: Relative transmission of a VPT faceplate at $\sim$ 420 nm after proton irradiation at the Proton Synchrotron. The relative response has been calculated after folding with the emission spectrum of Lead Tungstate .

13 Crystal Hadron Damage

As explained in Section 1.2, the main mechanism expected to lead to substantial response loss, and the need for detector replacement, is the hadronic damage inflicted upon the Lead Tungstate crystals. High energy hadrons can

collide with atoms in the lattice and produce multiple highly charged fragments that travel through the crystal for several microns disturbing and creating permanent colour centres in the crystal lattice as they propagate.

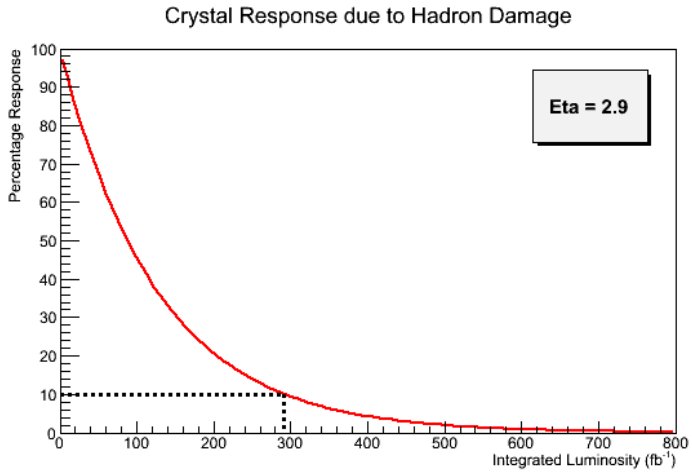

Figure 36: Lead Tungstate crystal light yield as a percentage of original value as a function of integrated luminosity at $\eta = 2.9$ due to hadron damage.

Figure 36 shows the predicted relative light yield of the crystals against integrated luminosity for η = 2.9 calculated using Equations 5 - 7. The light yield of the crystals at η = 2.9 reaches 10% of the original crystal light yield at an integrated luminosity of 290 fb^{-1}. This integrated luminosity is expected approximately half way through 2022 running, as shown in Table 12.

Equation 5 gives the relative light yield of the crystal, where LY is the crystal light yield, LY$_0$ is the original crystal light yield, μ_{ind} is the induced absorbance due to proton fluence and l is the crystal length in meters. Equation 6 describes μ_{ind}, the induced absorbance in the crystal due to a proton fluence Φ. A fluence of $\Phi = 2.7 \times 10^{13}$ cm^{-2} is expected for an integrated luminosity of 500 fb^{-1} at $\eta = 2.5$ for a collision energy of 13 TeV. Translating this fluence to different regions of η can be accomplished using Equation 7 and the co-efficients stated in Table 11, where F/F_0 is the scaling factor required [17].

$$\frac{LY}{LY_0} = e^{-\mu_{ind} \cdot l} \tag{5}$$

$$\mu_{ind} = 2.08 \times 10^{-13} \cdot \Phi^{1.0049} \tag{6}$$

$$\frac{F}{F_0} = \frac{e^{a+b\eta+c\eta^2}}{e^{a+b\cdot 2.5+c\cdot 2.5^2}} \tag{7}$$

Co-efficient	Value
a	-13.5112
b	7.913860
c	-0.998649

Table 11: Equation 7 co-efficients.

14 Laser Data Deconstruction

The laser data encapsulates the total response losses of the detector [14]. To evaluate the crystal transparency losses due to dose rate (crystal dE/dx losses), we must first remove the VPT conditioning, VPT faceplate losses

and crystal hadronic losses from the laser data. This is done by calculating the integrated VPT cathode current and dose from the integrated luminosity and combining this with the fits generated for VPT conditioning in Figure 34, VPT faceplate losses in Figure 35, and crystal hadron damage in Figure 36. The laser data is averaged over bands of 0.3 in pseudorapidity (η). An average value of η for any given band was used when determining the radiation fields, VPT gain and quantum efficiency, magnetic field adjustment and crystal light yield.

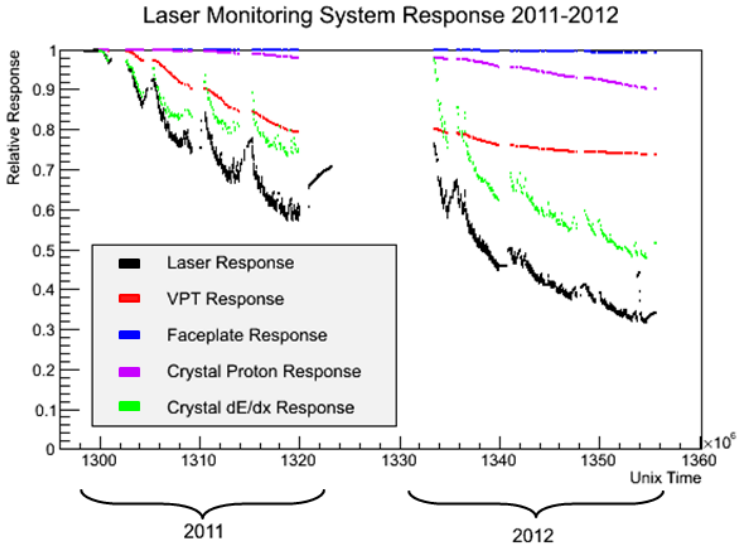

Figure 37: Relative response of all 4 response loss components throughout 2011-2012 and total response observed by the laser monitoring system for $2.7 < \eta < 3.0$ for a total integrated luminosity of 29.4 fb^{-1}.

Combining all of this information, we obtain the results shown in Figure 37, which shows the breakdown of the response loss components for the $2.7 < \eta < 3.0$ band during 2011 and 2012. The crystal dE/dx transparency losses and VPT conditioning are seen to be the largest factors in the detector response loss. The reduction in crystal transparency reduces the generation of VPT cathode current and is taken into consideration. The total integrated luminosity observed during this period is 29.4 fb^{-1}. The rate of VPT annealing between 2011 and 2012 is taken to be the equivalent of 10% per annum.

15 Projected Detector Response Losses

We now project forward to the end of LHC Run 3 in 2022. To do this we have used the integrated luminosities shown in Table 12 taken from the current LHC running expectations [18]. In the years with full running, integrated luminosity is evenly distributed over 7 month running periods. However, the shorter running period in 2018 is taken to be over 4 months. The total integrated luminosity for Run 1 (2011-2012) is 29.4 fb^{-1} at 7-8 TeV, corresponding to 20.8 fb^{-1} at 13 TeV. The total integrated luminosity for Run 2 (2015-2018) is 124 fb^{-1} and the total integrated luminosity for Run 3 (2020-2022) is 162 fb^{-1}. Long Shutdown (LS) periods are assumed to have zero luminosity.

Year	Run/LS	Int Lumi (fb^{-1})	Cumulative Int Lumi (fb^{-1})
2011	Run 1	6.1	4.3*
2012	Run 1	23.3	20.8*
2013	LS 1	0	20.8
2014	LS 1	0	20.8
2015	Run 2	30	51
2016	Run 2	40	91
2017	Run 2	36	127
2018	Run 2/LS 2	18	145
2019	LS 2	0	145
2020	Run 3	54	199
2021	Run 3	54	253
2022	Run 3	54	307

Table 12: Integrated luminosity per year and cumulative integrated luminosity for Run 1 LHC operation and the expected values for future running for Run 2 and Run 3. * 13 TeV equivalent.

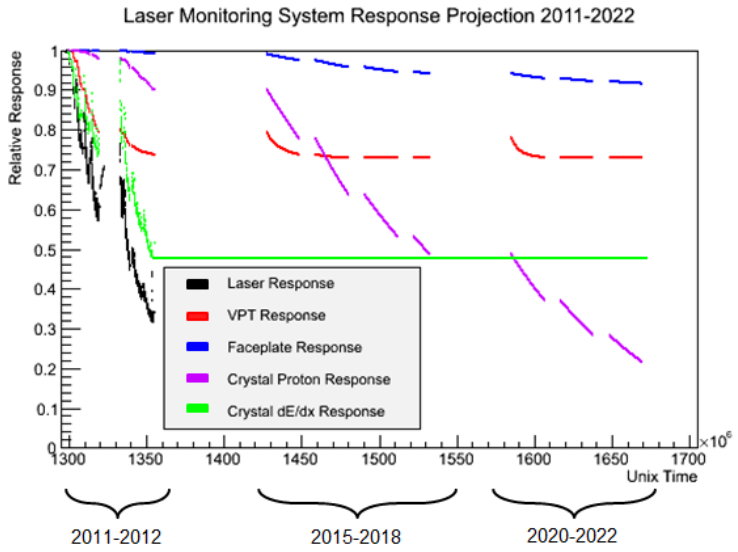

Figure 38: Relative response of the 4 response loss components and total response observed by the laser monitoring system for $2.7 < \eta < 3.0$ throughout 2011-2012 and projected forward to LS3, to end 2022. Total integrated luminosity predicted = 306.8 fb^{-1}. The crystal dE/dx transmission losses are assumed constant, as shown by the horizontal line, from end 2012 onwards.

Response loss predictions for $2.7 < \eta < 3.0$ are shown in Figure 38. Predictions of the transmission losses due to dE/dx are not possible since this depends on the LHC dose rate, with many crystals expected to be close to the point of saturation. Hadronic crystal damage losses become greater than VPT conditioning losses during Run 2 since the VPT conditioning losses saturate. By the start of Run 3, the light yield loss due to hadron damage is greater than the dE/dx losses seen at the end 2012. Faceplate response loss is also seen to be close to reaching an asymptotic level by the end of Run 3. VPT conditioning annealing of 10% per annum has been implemented during the shut down periods between runs [7].

If we assume the crystals are close to the point of dE/dx transmission loss saturation by the end of Run 1, and therefore take a crystal dE/dx relative response at the end of Run 3 of 47.8%, we estimate an average detector response of 6.9% for the $2.7 < \eta < 3.0$ band, by the end of 2022, with respect to the start of LHC running in 2010. However, the radiation field is known to be approximately 50% greater at $\eta = 2.9$ relative to the average η for this band of $\eta = 2.78$. Therefore we expect the total detector response at $\eta = 2.9$ to be only 3.5% with respect to the start of running in 2010. The observed and predicted levels of detector response at the end for each run are given in Table 13 for $2.7 < \eta < 3.0$.

	Relative Response %		
	Run 1	Run 2	Run 3
VPT Faceplate Response	99.2	94.1	91.6
VPT Conditioning Response	73.8	72.9	72.9
Crystal Hadron Damage Response	90.3	48.7	21.7
Crystal dE/dx Transmission Response	47.8	47.8	47.8
Total Detector Response	31.6	16.0	6.9

Table 13: Average total detector response loss and individual detector response loss components, at the completion of Phase 1 LHC runs for the $2.7 < \eta < 3.0$ band.

16 Crystal dE/dx Transmission Loss

The crystal dE/dx transmission losses have already surpassed the levels at which they were expected to saturate [19]. Figure 39 shows the relative crystal dE/dx transmission response, after subtracting the faceplate, conditioning and expected hadron damage from the laser data, against peak luminosity for fills in 2011 and 2012. Data further than 1 hour away from the beginning of a fill, or for fills shorter than 5 hours, were not included.

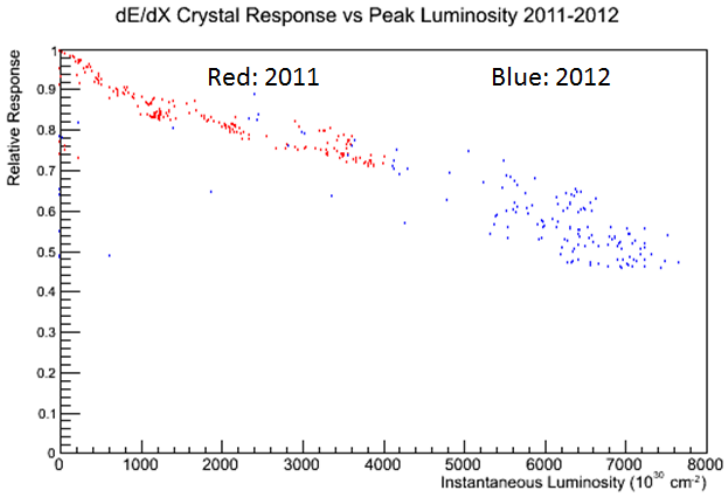

Figure 39: Calculated crystal dE/dx transmission response loss for 2011 and 2012 versus peak fill luminosity. Fills shorter than 5 hours in duration were not included.

Towards the end of 2012 running (the blue data in Figure 39) we potentially see a slight flattening with respect to increasing peak instantaneous luminosity. This could be evidence of dE/dx tranmission loss saturation. We note that laser data from individual VPTs and crystals at $\eta = 2.9$ would provide more conclusive evidence due to the significantly higher radiation fields in this region, these data are now in hand and is a topic for future investigation.

17 Relative Laser Response and dE/dx Transmission Loss Saturation

To investigate the possibility of dE/dx transmission loss saturation further we have compared the relative laser response for the 5 bands of pseudorapidity, of width 0.3 in η, that cover each end cap, for a number of fills throughout Run 1. We have normalised each band by subtracting the value of the last data point prior to each fill. The horizontal blue arrow indicates the duration of the fill with Unix time in seconds.

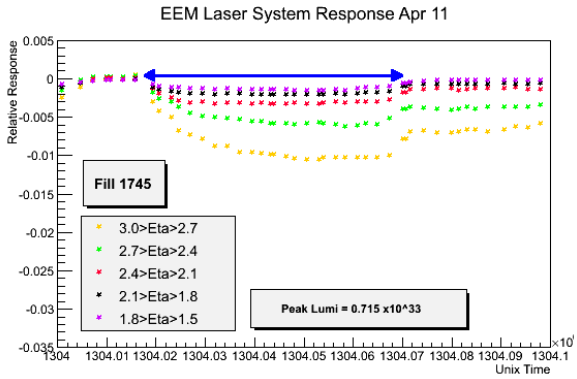

Figure 40: Relative laser response for April 2011, fill 1745, for the EEM. Peak luminosity observed $= 0.715 \times 10^{33}$ cm^{-2}s^{-1}.

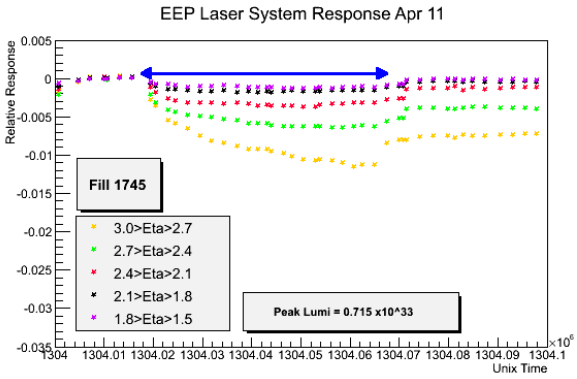

Figure 41: Relative laser response for April 2011, fill 1745, for the EEP. Peak luminosity observed $= 0.715 \times 10^{33}$ cm^{-2}s^{-1}.

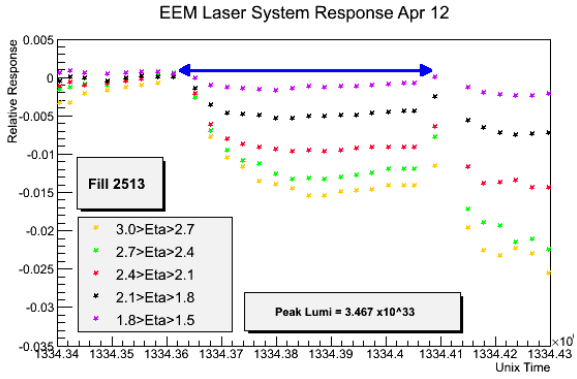

Figure 42: Relative laser response for April 2012, fill 2513, for the EEM. Peak luminosity observed $= 3.467 \times 10^{33}$ cm^{-2}s^{-1}.

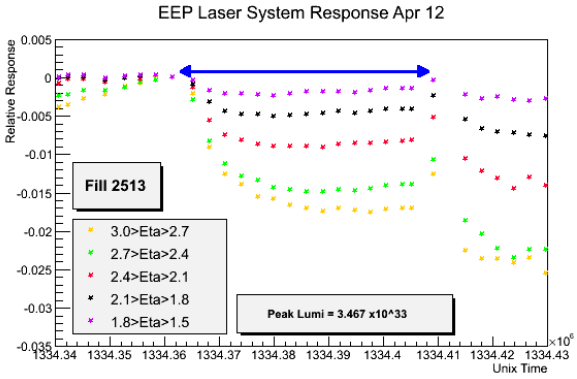

Figure 43: Relative laser response for April 2012, fill 2513, for the EEP. Peak luminosity observed $= 3.467 \times 10^{33}$ cm^{-2}s^{-1}.

In Figures 40 and 41, for EEM and EEP in April 2011, the level of relative response loss increases, as expected, with pseudorapidity. The yellow band of $2.7 < \eta < 3.0$ shows the greatest loss in both EEM and EEP. This is expected due to the exponential increase in radiation field, and therefore electromagnetic dose rate, towards the beam pipe and higher values of pseudorapidity.

Moving forward to April 2012, Figures 42 and 43 continue to show that the laser response losses are in order of pseudorapidity. However, the inner yellow band of $2.7 < \eta < 3.0$ may be displaying the first signs of saturation as it is much closer to the green band of $2.4 < \eta < 2.7$. The continued drop in response after the fill, at 1334.15×10^6 on the x axis, is due to the following fill starting soon after fill 2513 is completed.

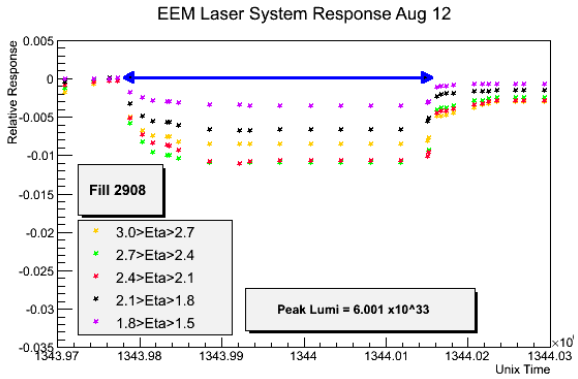

Figure 44: Relative laser response for August 2012, fill 2908, for the EEM. Peak luminosity observed $= 6.001 \times 10^{33}$ cm^{-2}s^{-1}.

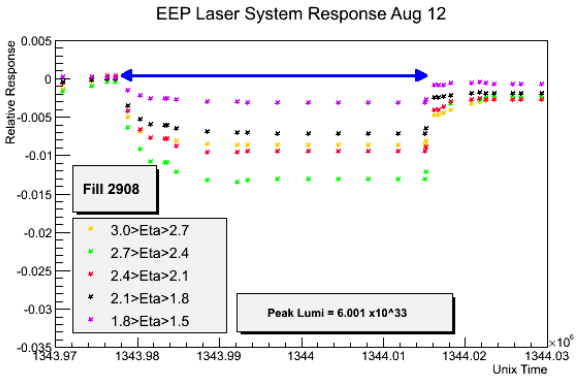

Figure 45: Relative laser response for August 2012, fill 2908, for the EEP. Peak luminosity observed $= 6.001 \times 10^{33}$ cm^{-2}s^{-1}.

For August 2012, we start to see the first definitive signs of dE/dx transmission loss saturation in Figures 44 and 45. The yellow band of $2.7 < \eta < 3.0$ is now displaying less loss than the green band of $2.4 < \eta < 2.7$ and the red band of $2.1 < \eta < 2.4$, for both endcaps. The peak luminosity for this fill is 6×10^{33} s^{-1}cm^{-2}, which is 76% greater than that seen during April 2012. In the EEM, the red band of $2.1 < \eta < 2.4$ is also similar in response to the green band of $2.4 < \eta < 2.7$. This is not yet seen in the EEP.

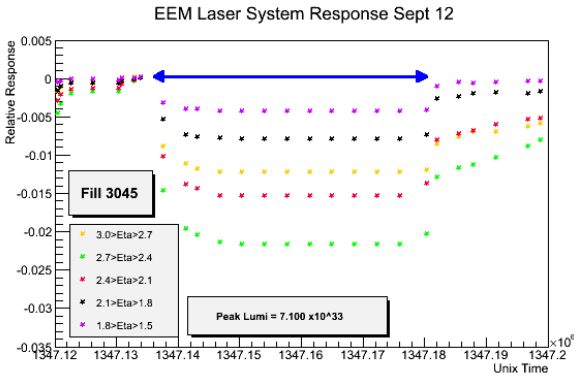

Figure 46: Relative laser response for September 2012, fill 3045, for the EEM. Peak luminosity observed $= 7.100 \times 10^{33}$ cm^{-2}s^{-1}.

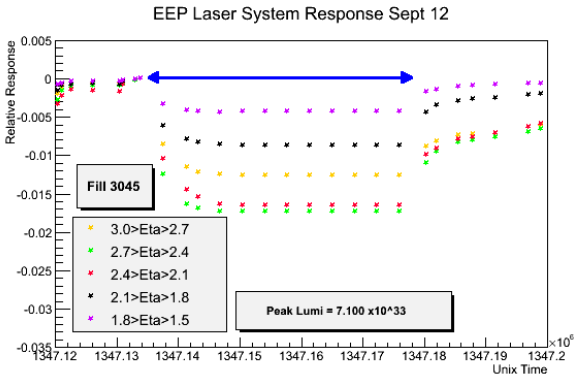

Figure 47: Relative laser response for September 2012, fill 3045, for the EEP. Peak luminosity observed $= 7.100 \times 10^{33}$ cm^{-2}s^{-1}.

Figures 46 and 47 show the relative response loss during September 2012 for a peak luminosity of 7.1×10^{33} cm^{-2}s^{-1}. The yellow band demonstrates less loss than the red and green bands in both endcaps. The red and green bands again show a significant difference in relative response to each other across the 2 endcaps. However, EEP displays much less difference between the 2 bands, unlike the August 2012 data, where this effect was only seen in EEM.

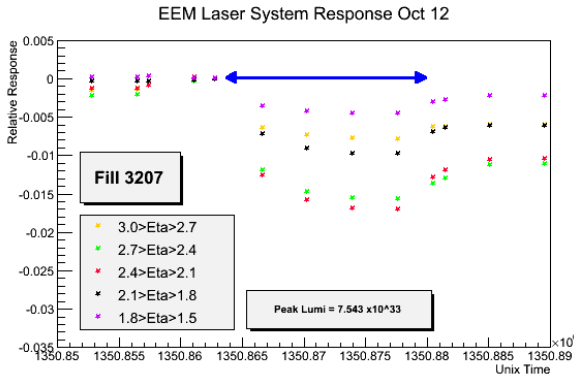

Figure 48: Relative laser response for October 2012, fill 3207, for the EEM. Peak luminosity observed $= 7.543 \times 10^{33}$ cm^{-2}s^{-1}.

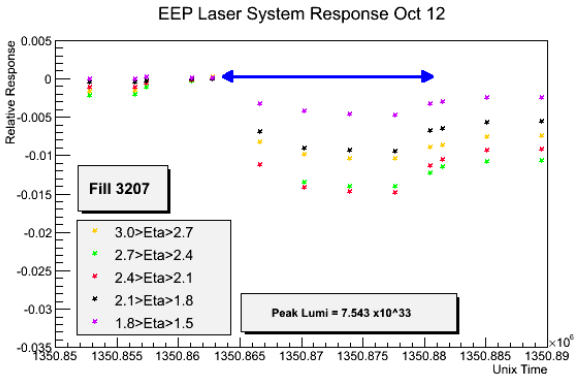

Figure 49: Relative laser response for October 2012, fill 3207, for the EEP. Peak luminosity observed $= 7.543 \times 10^{33}$ cm^{-2}s^{-1}.

In October 2012 the trend continues as the yellow bands in Figures 48 and 49 are now showing very similar losses to the black band of $1.8 < \eta < 2.1$. It is striking that the innermost part of the detector is now only suffering relative losses that are at the same level as the outer regions of the detector. This is a strong indication that dE/dx transmission losses have saturated in the inner region. The yellow band in EEM displays slightly less loss than the black, and slightly more loss in EEP. The green and red are again very similar in response loss with the red displaying slightly more loss than the green in both endcaps.

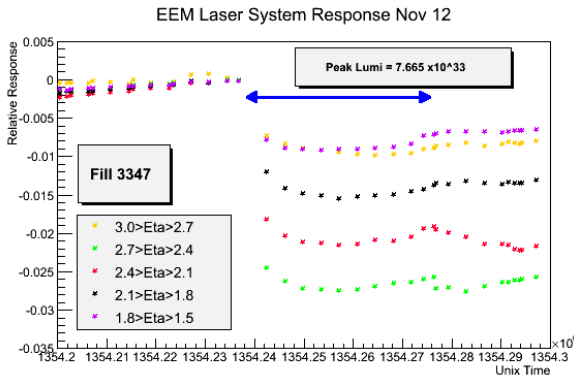

Figure 50: Relative laser response for November 2012, fill 3347, for the EEM. Peak luminosity observed $= 7.665 \times 10^{33}$ cm^{-2}s^{-1}.

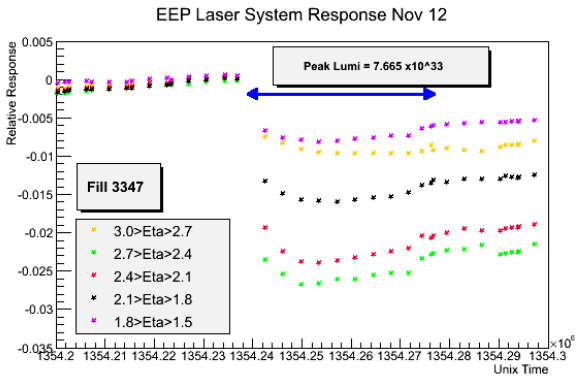

Figure 51: Relative laser response for November 2012, fill 3347, for the EEP. Peak luminosity observed $= 7.665 \times 10^{33}$ cm^{-2}s^{-1}.

Finally in late November 2012 we see the clearest demonstration of crystal dE/dx transmission response loss saturation in Figures 50 and 51. The yellow band now displays only slightly more loss than the outer most band of $1.5 < \eta < 1.8$ in both endcaps. The relative response between green and red bands no longer demonstrate any potential signs of saturation in this longer more defined fill. However, the red band of $2.1 < \eta < 2.4$ for the EEM appears to descend after the fill is completed. This is not expected and is not seen in any other bands of pseudorapidity in either endcap.

The three fills from September to November are very similar in peak luminosity. However, it is important to note that the intensity, duration and proximity in time of the prior fills to the fill under study will have a significant effect since this determines the level of annealing and saturation prior to each fill.

The sustained trend of reducing relative response loss seen throughout 2012 running in the innermost yellow band of $2.7 < \eta < 3.0$ provides strong evidence to suggest that there is saturation occurring in the Lead Tungstate dE/dx transmission response losses. Therefore the assumption to use the crystal dE/dx tranmission response at the end of Run 1 to calculate final detector response for Runs 2 and 3 can be considered reasonable for $2.7 < \eta < 3.0$.

18 Detector Energy Resolution

The target of the ECAL design was to measure the Higgs mass, for a Higgs at ∼100 GeV, with a resolution of better than 1 GeV. The CMS ECAL was designed to detect $H \rightarrow \gamma\gamma$ decays. These decays involve transverse photon energies of ∼50 GeV.

The mass resolution for a two particle decay is given by Equation 8, where $\frac{\sigma_E}{E}$ is the energy resolution of each photon. In order to achieve a 1% mass resolution, the photons must be measured with a resolution of better than $\sim 1.4\%$. Any detector response losses which cause this resolution to be substantially degraded would give rise to the need for detector replacement.

$$\frac{\sigma_M}{M} = \frac{1}{2}\left[\frac{\sigma_{E_1}}{E_1} \oplus \frac{\sigma_{E_2}}{E_2}\right] \tag{8}$$

The tracker acceptance only extends to η=2.5, which is outside the $2.7 < \eta < 3.0$ pseudorapidity band. The inner most band used for physics analysis is $2.4 < \eta < 2.7$ and this region is considered here. The average value of pseudorapity for this band is $\eta = 2.5$. In the EE, at a pseudorapidity value of 2.5, a photon with a transverse energy of 50 GeV from a 100 GeV Higgs decay has an energy of ∼300 GeV. This will be used as a reference energy for the following discussion.

The ECAL Endcap energy resolution has been measured in a test beam. It is parametrized by Equation 9, where a is the stochastic term, σ_n is the noise term, c is the constant term and E is the energy in GeV [1]. The values for these parameters are listed in Table 14 [20].

$$\frac{\sigma}{E} = \frac{a}{\sqrt{E}} \oplus \frac{\sigma_n}{E} \oplus c \tag{9}$$

Co-efficient	Value
a	0.052
σ_n	150 MeV
c	0.0038

Table 14: The values of the co-efficients for Equation 9, measured at a test beam and in CMS. σ_n is the total incoherent transverse noise per 3×3 crystal array.

For a 300 GeV particle, using Equation 9, we calculate an energy resolution of 0.49% before any detector response losses. The stochastic term contributes 0.30%, the noise term contributes 0.05% and the constant term contributes 0.38%. At high energies the constant term dominates Equation 9 as the stochastic and noise terms become negligible. The evolution of the energy resolution as a function of energy for a 3×3 crystal array is shown in Figure 52 for electrons at a test beam impinging on the central area of a crystal. Test beam measurements were obtained for 26 groups of 3×3 crystals. The summation over 3×3 arrays is needed due to the crystal Moliere radius of 2.1 cm, the radius of particle showers in the crystals. The crystals are 3×3 cm^2 in size and so a certain amount of energy spills out of the struck crystal and into its immediate neighbours [1]. This energy is included by carrying out the 3×3 summation.

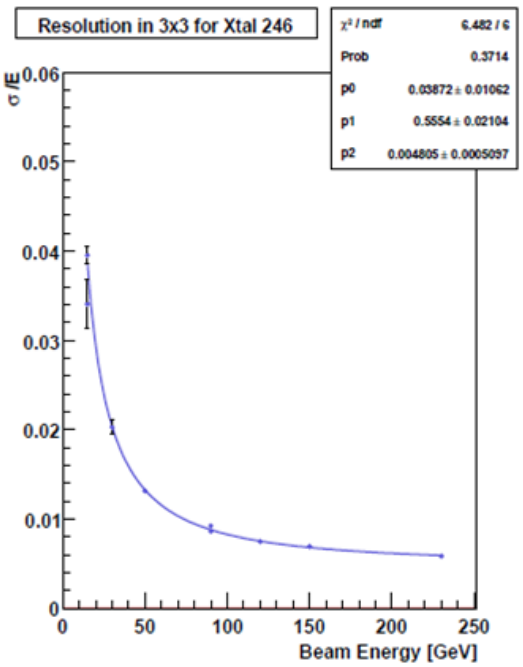

Figure 52: Fractional ECAL Endcap detector energy resolution of a 3×3 crystal array as a function of beam energy, using electrons [20].

From Figure 53 in appendix C, assuming dE/dx transmission loss saturation has been achieved by the end of Run 3, the total detector response will be reduced to 11.1% over the $2.4 < \eta < 2.7$ pseudorapidity range. This means the detector signal has a reduction factor, R, of 9.0. A 300 GeV particle now appears to have the same signal size as a lower energy 300/R GeV particle before the onset of response losses. The stochastic term increases by a factor of $\sqrt{\text{R}}$ and the noise term increases by a factor of R. The stochastic term now contributes 0.90% and the noise term contributes 0.45%.

As the crystal response lessens, and they become damaged, an additional constant term of $0.0025 \times \mu_{ind}$, where μ_{ind} is that described in Equation 6, must be added in quadrature as the light collection along the crystal becomes non-uniform. The total constant term now contributes 1.15%. This results in a total detector energy resolution for the $2.4 < \eta < 2.7$ band of 1.53%.

The result of the detector response losses on the energy resolution of the detector means that by the end of Run 3 in 2022 observations of $H \rightarrow \gamma\gamma$ and $H \rightarrow ZZ$ will still be possible for physics analysis. However, for High Luminosity LHC running beyond 2022, for Phase 2 the photon resolution will degrade and be progressively worse than the target resolution of 1.4%. As a consequence a detector replacement will need to be designed and then installed during LS3.

19 Conclusions

The focus of this analysis was to determine when a replacement of the CMS ECAL Endcap would be required by performing an analysis of the detector response loss components in order to inform the detector replacement discussions which are currently on going.

The VPT currents from both the PVSS and CAEN systems have been measured and the correspondence and agreement determined between specific PVSS and CAEN channels. The detector properties that influence the instantaneous current produced by each VPT have been analysed. This has enabled the α co-efficient to be evaluated from Equation 3. VPT photo-cathode currents and the corresponding levels of VPT conditioning have been estimated for LHC running in 2011 and 2012.

By combining measurements of integrated luminosity with experimental data from the test rigs at Brunel and UVa the VPT conditioning levels have been determined in CMS. Measurements of Lead Tungstate hadron damage from the Proton Synchotron at CERN, combined with integrated luminosity measurements, have enabled the light

yield loss in the crystals, due to hadron damage, to be calculated. The loss of transparency, and therefore photon transmission, of the VPT faceplates has also been determined from measurements from the CERN Proton Synchotron and integrated luminosity measurements. The total detector response observed by the laser monitoring system has been deconstructed into its individual response loss components enabling the calculation of crystal dE/dx transmission response losses to be calculated for LHC Run 1.

Predictions of the expected integrated luminosity for each year of Phase 1 LHC running were used to estimate the behaviour of each of the individual response loss components until the end of LHC Run 3 in 2022. It was found that the crystal hadron damage becomes the dominant factor in determining the longevity of the detector. The average total predicted EE detector response over the inner most band of $2.7 < \eta < 3.0$ by the end of Run 3 is just 6.9% of the detector's original response.

The crystal dE/dx transmission level of 47.8% surpasses the previously predicted saturation level of 69%. Potential evidence of crystal colour centre saturation due to electromagnetic dose at large values of pseudorapidity prompted further investigation. The first strong evidence of saturation over the $2.7 < \eta < 3.0$ band was seen by performing a comparison between the relative laser response over all 5 bands in units of 0.3 in pseudorapidity that cover each end cap.

The energy resolution of the EE is affected by the response losses of the detector as described in Section 18. As such the energy resolution, for a 50 GeV transverse energy photon at a pseuodrapidity of 2.5, is reduced from 0.49% before Run 1 to 1.53% by the end of Run 3 for $2.4 < \eta < 2.7$. This is only marginally worse than the required 1.4% resolution required for a Higgs mass resolution of $\sim$1 GeV. This loss of resolution will have only a moderate effect on detector performance and the ability for further physics analysis to be performed. However, for Phase 2 LHC running beyond 2022 a significant worsening of detector performance is to be expected due to crystal hadron damage as the integrated luminosity during Phase 2 LHC operation from 2025 to 2035 is expected to be 10 times greater than that during Phase 1 operation. The replacement of the inner most regions of the detector, or the entire detector, with a more radiation hard solution during Long Shutdown 3 will be required.

References

[1] CMS Collaboration, *The Electromagnetic Calorimeter Project: Technical Design Report*, Technical Report CERN/LHCC-97-33, CMS-TDR 4 (1997), http://cdsweb.cern.ch/record/349375

CMS Collaboration, *The CMS experiment at the CERN LHC*, 2008 JINST 3 S08004, http://dx.doi.org/10.1088/1748-0221/3/08/S08004

[2] A N Annenkov et al., *Radiation damage kinetics in $PbWO_4$ crystals*, CMS Note 1997/009

[3] M Huhtinen et al. *High-energy proton induced damage in $PbWO_4$ calorimeter crystals*, NIM-A 545 (2005) 63-87

[4] E. Auffray, M. Korjik, Member, IEEE, and A. Singovski, on behalf of CMS-ECAL Group, *Experimental Study of Lead Tungstate Scintillator Proton-Induced Damage and Recovery*, IEEE TRANSACTIONS ON NUCLEAR SCIENCE, VOL. 59, NO. 5, OCTOBER 2012 2219

[5] K. W. Bell et al. *Vacuum Phototriodes for the CMS Electromagnetic Calorimeter Endcap*, IEEE TRANSACTIONS ON NUCLEAR SCIENCE, VOL. 51, NO. 5, OCTOBER 2004

[6] R M Brown, *EE Photodetectors for SLHC*, FNAL 20/1108 (2008), Slide 12-13

RCA Corporation, *RCA Handbook*, Fig 54 - 55, http://psec.uchicago.edu/links/Photomultiplier_Handbook.pdf

[7] D Leslie, *News and VPT test plans for 2011 at Brunel*, EE operation and test beam meeting, 13 Jan 2011, https://indico.cern.ch/event/119834/

[8] P. Hobson, *Results from VPT faceplate irradiations*, EE operation and test beam meeting, 9 Feb 2012, https://indico.cern.ch/event/177027/

[9] Dawn Elizabeth Leslie et al., *The effect of pulse rate on VPT response and the use of an LED light to improve stability*, Presented at ICATPP09: 11th ICATPP Conference on Astroparticle, Particle, Space Physics, Detectors and Medical Physics Applications, https://cds.cern.ch/record/1358790/files/CR2009_284.pdf

[10] CMS Collaboration, *Performance and operation of the CMS electromagnetic calorimeter*, 2010 JINST 5 T03010,http://iopscience.iop.org/1748-0221/5/03/T03010/pdf/1748-0221_5_03_T03010.pdf

[11] R.M Brown, *The variation in response of the CMS ECAL vacuum phototriodes as a function of orientation in a strong magnetic field*, CMS NOTE -2009/014, http://cms.cern.ch/iCMS/jsp/openfile.jsp?type=NOTE&year=2009&files=NOTE2009_014.pdf

[12] Alexander Ledovskoy, 2013/11/08, https://twiki.cern.ch/twiki/pub/Main/Point5Analysis/131108_pc_ledovskoy-doses-currents.pdf

[13] http://www.cern.ch/cms-fluxmap

[14] CMS Collaboration, *ECAL detector performance plots*, CMS-DP-2013/007 (2012), https://twiki.cern.ch/twiki/pub/CMSPublic/EcalDPGResultsCMSDP2013007/histories_2011-2012.pdf

[15] Bruce Kennedy, *CMS Ecal Endcap Geometry Specification*, CMS NOTE-2000/029

[16] John Garland Wood, *VPT Response Evolution Studies*, ECAL DPG Workshop, 21/11/2013, https://indico.cern.ch/event/272171/

[17] S. Ledovskoy, *Dose maps, Magnetic field correction factor*, file131108_pc_ledovskoy.pdf, 8 Nov 2013.

S. Ledovskoy, *Hadron damage, induced absorption and light loss*, ECAL Upgrade meeting, 18 Oct 2011, https://indico.cern.ch/event/157097/

[18] J. Wenninger, *Integrated performance of the LHC at 25 ns without and with LINAC4, Review of LHC and Injector Upgrade Plans Workshop*, 29-31 Oct 2013, Archamps, https://indico.cern.ch/event/260492/

[19] D Cockerill, *Estimates for the changes in light yield from the CMS ECAL during LHC operation*, CMS IN-2010/026

[20] S. Beauceron, P.Bloch, *Studies of the Ecal Endcap Energy Resolution using 2007 Test Beam Data* CMS DN-2009/002

Appendices

A Magnetic Field Adjustment Factors

Table 15 gives the data points used to generate Figure 28, taken from Sasha Ledovskoy's paper [12] pages 4 and 6. θ is taken to be the angle between interaction point, VPT and beam pipe.

θ	Adjustment Factor
0.099	0.679
0.110	0.689
0.121	0.700
0.134	0.713
0.148	0.731
0.164	0.745
0.181	0.759
0.200	0.784
0.221	0.796
0.244	0.808
0.269	0.825
0.297	0.840
0.328	0.846
0.361	0.849
0.398	0.842
0.439	0.825

Table 15: Magnetic field adjustment factor data [12].

B VPT Anode Current Benchmarks

The dates at which a VPT anode current of 10 mC is accumulated for each of the pseudorapidity bands are given in Table B. The effect of crystal light yield loss throughout operation has not been included. Therefore 10 mC is expected to be achieved slightly later than the dates given in Table B. As a comparison, if crystal light yield loss is accounted for, 10 mC of anode current is accumulated by 16/09/2012.

Pseudorapidity Band	10 mC Achieved No Sooner Than
$2.7 < \eta < 3.0$	22/08/2012
$2.4 < \eta < 2.7$	25/11/2012
$2.1 < \eta < 2.4$	31/05/2016
$1.8 < \eta < 1.5$	02/05/2022

Table 16: Dates at which 10 mC of VPT anode current have been accumulated for bands of 0.3 units of pseudorapidity. Effects of crystal light yield loss is not included in the calculations.

C Laser Data Deconstruction, Additional η Bands

Figures 53, 54 and 55 show the deconstruction of the laser data into the four response loss components over the bands of pseudorapidity, 2.7 to 2.4, 2.4 to 2.1 and 2.1 to 1.8 respectively, for 2011 and 2012. The projected response loss components for Run 2, 2015-2018 and Run 3, 2020-2022, are also shown.

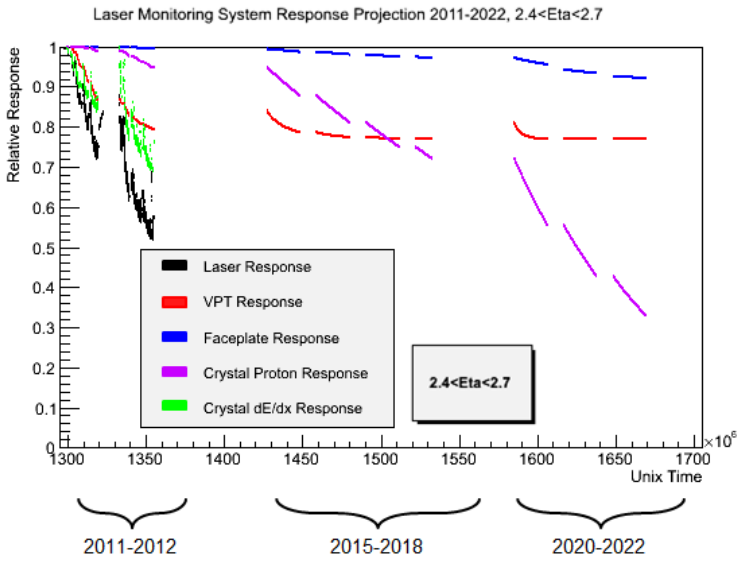

Figure 53: Relative response of the 4 response loss components and total response observed by the laser monitoring system for $2.4 < \eta < 2.7$ throughout 2011-2012. Losses due to conditioning, faceplate damage and hadron damage are projected forward to LS3, to end 2022. Total integrated luminosity predicted = 306.8 fb^{-1}.

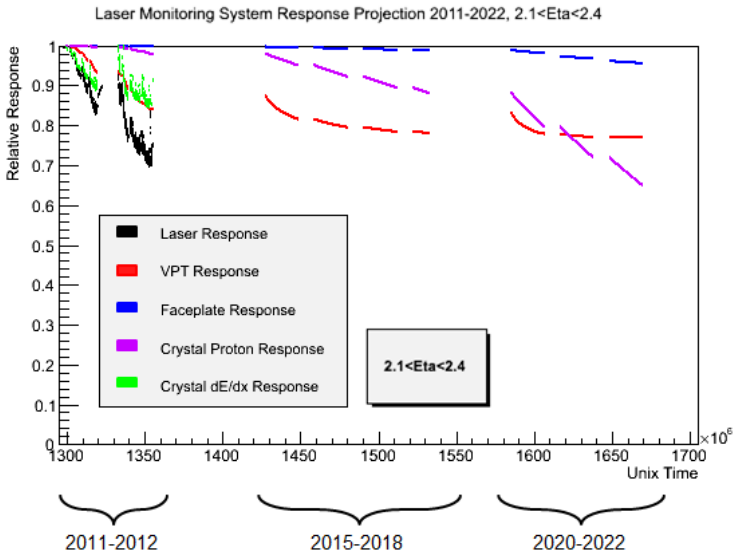

Figure 54: Relative response of the 4 response loss components and total response observed by the laser monitoring system for $2.1 < \eta < 2.4$ throughout 2011-2012. Losses due to conditioning, faceplate damage and hadron damage are projected forward to LS3, to end 2022. Total integrated luminosity predicted = 306.8 fb^{-1}.

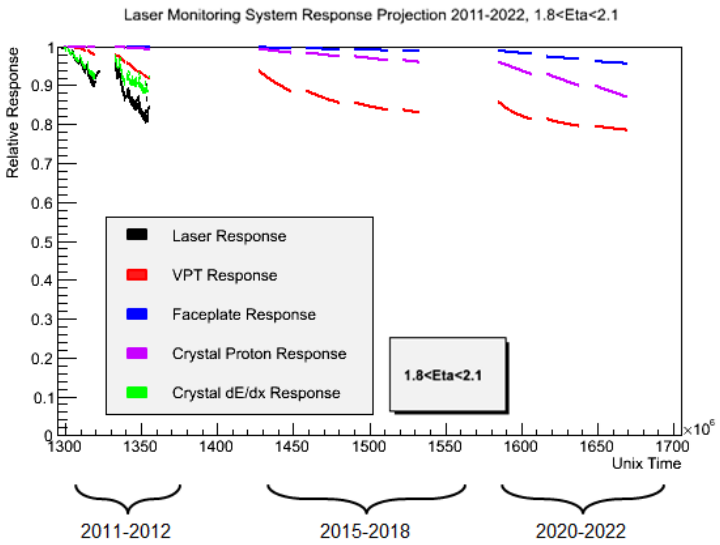

Figure 55: Relative response of the 4 response loss components and total response observed by the laser monitoring system for $1.8 < \eta < 2.1$ throughout 2011-2012. Losses due to conditioning, faceplate damage and hadron damage are projected forward to LS3, to end 2022. Total integrated luminosity predicted = 306.8 fb^{-1}.

D Plot Generating Scripts

The scripts used to create the plots throughout the paper are listed in Table 17.

Figure	Script Name
8	FillFitWideBaselinePNov12.C
9	FillFitWideBaselinePNov12.C
10	PVSSBaselinePNov12.C
13	AnoCodeAnalyserMk2N.C
14	AnoCodeAnalyserMk2P.C
15	CAENChannelCompareDee1.C
16	CAENChannelCompareDee2.C
17	CAENChannelCompareDee3.C
18	CAENChannelCompareDee4.C
19	PVSSandCAENNov12Dee1Ch1.C
20	PVSSandCAENNov12Dee1Ch1.C
21	LumiNov12UnixtTestMk2.C
22	LumiApr11unixtAdj.C
23	PVSSPNov12.C
24	PVSSPApr11.C
25	VPTGain.C
26	VPTQE.C
27	VPTLY.C
28	VPTPGMag.C
29	VPTPGMagRad.C
30	PVSSOverLumiAllMk2.C
31	PVSSOverLumiApr11Mk2.C
33	VPTCondFitMk3.C
34	VPTCondFitMk3.C
35	FPCondFit.C
36	PDamageFitMk2.C
37	LaserDataFutureEverythingMk4.C
38	LaserDataFutureEverythingMk4.C
39	dEdXvsPLumi.C
40	LaserDataComparisonEEMApr11
41	LaserDataComparisonEEPApr11
42	LaserDataComparisonEEMApr12
43	LaserDataComparisonEEPApr12
44	LaserDataComparisonEEMAug12
45	LaserDataComparisonEEPAug12
46	LaserDataComparisonEEMSept12
47	LaserDataComparisonEEPSept12
48	LaserDataComparisonEEMOct12
49	LaserDataComparisonEEPOct12
50	LaserDataComparisonEEMNov12
51	LaserDataComparisonEEPNov12
53	LaserDataFutureEverything2.6Mk3.C
54	LaserDataFutureEverything2.3Mk3.C
55	LaserDataFutureEverything2.0Mk3.C

Table 17: Name of the scripts used to generate the plots used throughout the report.